Universität Hamburg

Master Thesis

Supernova Neutrinos in LENA

Towards a Time- and Flavor-Resolved Analysis

Author:

Markus Kaiser

1. Supervisor:

Dr. Michael Wurm

2. Supervisor:

Prof. Dr. Caren Hagner

Group: Neutrino physics

Institut für Experimentalphysik

December 11, 2012

Abstract

The 50 kt liquid scintillator-based detector LENA (**L**ow **E**nergy **N**eutrino **A**stronomy) is an option proposed for a next-generation neutrino observatory. The combination of the liquid scintillator technique and huge detector dimensions will allow a high-statistics measurement of the neutrino signal from a core-collapse supernova (SN) within our galaxy. The key goal of studies on the SN neutrinos is to measure time- and flavor-dependent features of the neutrino signal.

Within this thesis, the event-based neutrino flavor identification for both the time-integrated and the time-dependent SN neutrino signal are analyzed. A strategy for identifying the neutrino flavor is enabled by the different SN neutrino detection channels provided by LENA. Efficiencies of event discrimination of these detection channels are calculated and presented in this thesis. Furthermore, studies of the flavor-dependent SN neutrino signal addressing the determination of the neutrino mass hierarchy are examined.

Zusammenfassung

Der 50 kt Flüssigszintillator-Detektor LENA (**L**ow **E**nergy **N**eutrino **A**stronomy) ist ein mögliches Neutrino-Observatorium der nächsten Generation. Die Kombination von Flüssigszintillator und großen Detektordimensionen erlaubt die Messung des Neutrino-Signals einer Kernkollaps Supernova (SN) innerhalb unser Galaxie mit hoher Statistik. Die Schlüsselidee von Studien zu SN Neutrinos ist es, zeit- und flavor-abhängige Charakteristiken des Neutrino-Signals zu messen.

Im Rahmen dieser Arbeit wird die ereignis-basierte Identifikation der Neutrino Flavor für das zeit-integrierte sowie das zeit-aufgelöste Neutrino-Signal analysiert. Eine Strategie zur Identifikation der Neutrino Flavor wird dadurch ermöglicht, dass LENA mehrere SN Neutrino Detektionskanäle bietet. Effizienzen zur Ereignis-Diskrimination der Detektionskanäle werden in dieser Arbeit ermittelt und vorgestellt. Des Weiteren werden Studien für das flavor-aufgelöste Signal zur Bestimmung der Neutrino Massenhierarchie untersucht.

Contents

Chapter 1

Introduction

In 1930, the neutrino was proposed by Wolfgang Pauli to solve, among other problems, the continuous energy spectrum observed for electrons from beta decays. 26 years later, Clyde Cowan and Frederick Reines proved the existence of the neutrino. One important topic of the following decades has been the measurements of the solar neutrino deficit, which finally led to the establishment of the neutrino oscillation concept. Alongside, other properties of the neutrinos such as different flavors were discovered. Today, neutrino physics is increasingly focused on the information that neutrinos carry about their sources. Since neutrinos only interact via the weak interaction, they can travel great distances without any interactions. Thus, they preserve the unscattered information of their production and serve as suitable messengers for the dynamics and the physical state of stars.

The next-generation neutrino observatory LENA[1] is one of three detector options proposed within the scope of the European LAGUNA[2] project. LENA is a liquid scintillator-based detector with a target mass of 50 kt. Hence, it would be the first experiment to combine the large dimensions of a detector like Super-Kamiokande [1] with the scintillator detection principle of experiments like Borexino [2] or KamLAND [3]. LENA is designed as a multi-purpose detector with a broad physics program, including measurements to study terrestrial, astrophysical and high-energy neutrino sources.

One important astrophysical neutrino source is a core-collapse supernova (SN), which is the final step in the lifetime of massive stars. SNe are very rare, as they only occur a few times per century within our galaxy. Thus, the measurement of a high-statistics neutrino signal from a SN would be an outstanding success. The field of neutrino astronomy has been promoted with the detection of neutrinos from the SN1987A. This neutrino signal included only a handful neutrinos, but even so contributed greatly to the understanding of SN and provided some limits in the field of particle physics.

Assuming a SN in the center of the Milky Way, the expected number of events detected in LENA would be about 10^4. Besides a low energy threshold and a superior energy resolution compared to water Cherenkov detectors like Super-Kamiokande, LENA provides

[1] Low Energy Neutrino Astronomy

[2] Large Apparatus for Grand Unification and Neutrino Astrophysics

several detection channels with different neutrino flavor sensitivities. The golden detection channel for SN neutrinos in LENA is the inverse beta decay, which is sensitive to the $\bar{\nu}_e$. Elastic scattering on protons primarily provides information on ν_μ and ν_τ, while interactions on ^{12}C and the elastic scattering on electrons carry also information on the ν_e. However, neutrino flavor identification requires efficient event discrimination of the different channels.

The focus of this thesis is on the analysis of channel discrimination. First of all, neutrino event rates and the visible neutrino energy spectra for the different detection channels in LENA are investigated. Based on these studies, a SN neutrino signal detected by LENA is simulated. The first approach of detection channel discrimination in LENA is conducted using the time-integrated signal. Subsequently, the analysis is applied to the time-dependent SN neutrino signal. Finally, studies of the flavor-dependent SN neutrino signal regarding the neutrino mass hierarchy are examined.

A dedicated analysis of a flavor- and time-resolved SN neutrino signal offers rich opportunities to address several topics concerning SN physics and particle physics. The standard SN explosion model leaves several open questions, such as the detailed sequence of the final break out, nucleosynthesis processes or cooling mechanisms of the proto-neutron star. In the case of particle physics one looks for robust features, that are as far as possible independent of the explosion model.

The structure of this thesis is as follows: Chapter 2 covers the properties of neutrinos and neutrino oscillations. Afterwards, chapter 3 introduces the explosion model of a SN and discusses the expected neutrino signal. The focus of chapter 4 is on the design of LENA and its broad physics program. Chapter 5 moves on to studies on event discrimination of the different detection channels and its efficiencies. Subsequently, some approaches of the flavor-dependent SN neutrino signal regarding the neutrino mass hierarchy are examined in chapter 6. Finally, chapter 7 gives a summary of this thesis, as well as an outlook on possible future research.

Chapter 2

Neutrino physics

In 1930, Wolfgang Pauli postulated a new particle to explain the continuous energy spectrum observed for electrons from beta decays. This continuous energy spectrum was in conflict with the mono-energetic electron expected from a two-body decay. The postulated particle should thus guarantee the conservation of energy and spin in the decay process. The measured beta decay spectra only allowed for a very light and electrically neutral particle, which therefore would be very hard to detect. Three years later, Enrico Fermi evolved the theory for the beta decay and named the postulated particle "neutrino"[1]. It took 26 years since the postulation from Pauli before Clyde Cowan and Frederick Reines were able to prove the existence of neutrinos in 1956. A few years later, Leon Lederman, Mel Schwartz and Jack Steinberger discovered that more than one type (flavor) of neutrino must exist. From the analysis of the Z^0 decay at colliders one can further derive that there are 3 ± 0.06 light active[2] neutrino flavors with masses smaller than half the Z^0 mass [4]. This chapter will give a short summary on neutrinos and describes their most important properties, with particular regard to supernova physics.

2.1 Neutrinos in the Standard Model

This section briefly summarizes the Standard Model of particle physics (SM). A more detailed introduction can be found in [5]. This section will focus on neutrinos and their properties. At present, the SM is impressively successful in describing the elementary particles and the fundamental interactions between them. It is based on a relativistic quantum field theory. The SM includes twelve elementary particles of spin $\frac{1}{2}$, called fermions, which are classified in table 2.1. They are divided into two basic categories, six leptons and six quarks. Furthermore, pairs of particles of both categories are arranged into three generations, where respective particles of each generation have similar properties. Finally, every fermion has a corresponding anti-particle, which leads to the doubling of

[1] Italian: "little neutral one"

[2] There is the possibility of additional so-called "sterile neutrinos", that do not couple to the Z^0. From now on, these "active neutrinos" will simply be called neutrinos.

the number of elementary particles.
The fundamental forces enable interactions between elementary particles. Particles can only interact via a distinct force, if they carry the respective charge. Three of the four known fundamental forces are described within the SM. It contains the electromagnetic, weak and strong interactions but does not cover gravitation. All fermions carry weak charge, but only quarks carry the strong charge also called "color charge". The electric charge (El. Charge) of the fermions is given in table 2.1. Mediation of forces is realized by the so-called gauge bosons with spin 1. A list of them is given in table 2.2.

	El. Charge	**1st Generation**		**2nd Generation**		**3rd Generation**	
Quarks	$+\frac{2}{3}$	Up	u	Charm	c	Top	t
	$-\frac{1}{3}$	Down	d	Strange	s	Bottom	b
Leptons	-1	Electron	e^-	Muon	μ^-	Tau	τ^-
	0	Electron neutrino	ν_e	Muon neutrino	ν_μ	Tau neutrino	ν_τ

Table 2.1: Classification of fermions in the Standard Model.

Interaction	**Gauge boson(s)**	**Mass of bosons [GeV]**
Strong	Gluons	0
Weak	W^+/W^-	80.4
	Z^0	91.2
Electromagnetic	Photon	0

Table 2.2: List of gauge bosons in the Standard Model.

Neutrinos are electrically neutral and have no strong charge, whereby they only interact via the weak interaction. Therefore they are able to travel long distances through matter without interactions. This property makes neutrinos on the one hand very hard to detect but on the other hand very valuable because they usually carry direct (unscattered) information about their sources.
In the SM, neutrinos are assumed to be massless, but the discovery of neutrino flavor oscillations (see Section 2.2) requires neutrinos to have a non-vanishing rest mass, meaning physics beyond the SM. At the moment however, the exact neutrino masses are unknown and the upper limits on neutrino masses are in the order of a few eV.
The SM states that there are three neutrinos, ν_e, ν_μ and ν_τ. They are described in the SM as the partner particles of the respective charged leptons. With the detection of the ν_τ in 2000, the third and last neutrino has been experimentally proofed. Neutrinos are described as Dirac spinors in the SM. However, it is still possible that neutrinos are their own anti-particles which then have to be described as Majorana particles. The probably only kind of experiment which can answer this question is the neutrinoless double beta decay [6].

2.2 Neutrino oscillations

The existence of neutrino masses opens up the possibility of neutrino oscillations. This phenomenon allows a neutrino, which has been created as a specific flavor state at one spatial point, to be measured as another flavor state at another point in space and time. Bruno Pontecorvo first proposed the idea of neutrino oscillation in 1957. The first evidence for neutrino oscillation came from the famous Homestake experiment of Ray Davis in the late 60s [7]. He observed a significantly smaller rate of solar (electron) neutrinos than the Standard Solar Model (SSM) predicted. In the following years, many other experiments confirmed this measurement which became known as the "Solar Neutrino Problem". These experiments were only able to measure electron neutrinos, which is the only neutrino flavor produced in solar fusion. Neutrino oscillation became quickly popular as a possible explanation for the measured deficit. Thus, the "missing" solar neutrinos could have been originally electron neutrinos which oscillated to other flavors along the way from the Sun to Earth and therefore could no longer be measured by the detectors. It took until 2001, when the Sudbury Neutrino Observatory (SNO) could finally confirm this concept of oscillating solar neutrinos [8]. SNO was able to detect separately both electron neutrinos as well as the sum of all neutrino flavors. It was found that the total sum of neutrinos agrees very well with the SSM predictions and that the amount of electron neutrinos is about 35% of all neutrinos. The following introduction on neutrino oscillations bases on [9], [10] and [11].

2.2.1 Neutrino oscillations in vacuum

This section gives an introduction on neutrino oscillations in vacuum. Neutrino oscillation can be completely explained in terms of the wave packet formalism. However, it is possible to obtain the same results with a simpler plane wave approximation as will be summarized here [12]. Neutrinos are always produced and detected in a (weak) flavor eigenstate $|\nu_\alpha\rangle$, where $\alpha = \mathrm{e}$, μ or τ. Simultaneously there are the neutrino mass eigenstates $|\nu_i\rangle$ with defined masses m_i. These are the eigenstates of the free Hamiltonian. Flavor eigenstates and mass eigenstates do not necessarily have to be identical, the other case allowing neutrinos to oscillate: A neutrino of flavor α can be described as a linear superposition of neutrino mass eigenstates:

$$|\nu_\alpha\rangle = \sum_i U^*_{\alpha i} |\nu_i\rangle \,, \tag{2.1}$$

where $U^*_{\alpha i}$ is a unitary mixing matrix known as the Pontecorvo-Maki-Nakagawa-Sakata (PMNS) Matrix. This mixing matrix is analogous to the Cabibbo-Kobayashi-Maskawa (CKM) matrix that describes the quark mixing. The inversion of this equation yields an

expression for the mass eigenstates in terms of the flavor eigenstates:

$$|\nu_i\rangle = \sum_\alpha U_{\alpha i} |\nu_\alpha\rangle \tag{2.2}$$

where $U_{\alpha i}$ is the conjugate of the matrix $U^*_{\alpha i}$.
In the case of three mass eigenstates and Dirac neutrinos the mixing matrix can be parameterized by three mixing angles θ_{ij} and one CP violating phase δ. If neutrinos are Majorana particles, two additional phases α_1 and α_2 are required. Following the standard parameterization U is given by:

$$U = \begin{pmatrix} 1 & 0 & 0 \\ 0 & c_{23} & s_{23} \\ 0 & -s_{23} & -c_{23} \end{pmatrix} \cdot \begin{pmatrix} c_{13} & 0 & s_{13}e^{-i\delta} \\ 0 & 1 & 0 \\ -s_{13}e^{+i\delta} & 0 & -c_{13} \end{pmatrix} \cdot \begin{pmatrix} c_{12} & s_{12} & 0 \\ -s_{12} & c_{12} & 0 \\ 0 & 0 & 1 \end{pmatrix} \cdot \begin{pmatrix} e^{i\frac{\alpha_1}{2}} & 0 & 0 \\ 0 & e^{i\frac{\alpha_2}{2}} & 0 \\ 0 & 0 & 0 \end{pmatrix}, \tag{2.3}$$

with the abbreviations $s_{ij} = \sin\theta_{ij}$ and $c_{ij} = \cos\theta_{ij}$. The mixing angles can take values in the range $0 \leq \theta \leq \pi$. The phase δ can take values in the range $0 \leq \delta \leq 2\pi$. In case of CP conservation in the lepton sector, δ equals zero. The Majorana phases effect lepton number violating processes like the neutrinoless double beta decay. Since the Majorana phases do not effect oscillation physics, they will be neglected from now on in this description.

The time evolution of a neutrino mass eigenstate is described by the Schrödinger equation. Generally, for a quantum state $|\Psi(t)\rangle$ the solution of the time-dependent Schrödinger equation has to be determined:

$$i\frac{\partial}{\partial t}|\Psi(t)\rangle = H|\Psi(t)\rangle \tag{2.4}$$

where H is the total Hamiltonian. The equation for a neutrino mass eigenstate in vacuum is solved by a plane-wave:

$$|\nu_i(t)\rangle = e^{-i(E_i t - \vec{p}\cdot\vec{x})} |\nu_i(0)\rangle \tag{2.5}$$

where E denotes the energy and p the momentum of the neutrino. Because of the small neutrino masses, the ultra-relativistic approximation, $p \gg m_i$ and $E \approx p$, is feasible. The energy eigenvalues of the mass eigenstates can be expressed as follows:

$$E_i = \sqrt{m_i^2 + p_i^2} \approx p + \frac{m_i^2}{2p} \approx E + \frac{m_i^2}{2E} \tag{2.6}$$

For convenience, the natural units are used ($\hbar = c = 1$) and the propagation distance L is introduced so that one can write $t \approx L = x$. This approximation allows to rewrite equation 2.5:

$$|\nu_i(t)\rangle = e^{-im_i^2 \frac{L}{2E}} |\nu_i\rangle \tag{2.7}$$

Evidently, the propagation of the eigenstate depends on the mass m_i and thus will be different for different m_i. The probability that a neutrino of flavor α will be observed after time t and propagation distance L as a neutrino of flavor β, is given by:

$$P(\alpha \to \beta) = |\langle \nu_\beta | \nu_\alpha(t) \rangle|^2 = \left| \sum_i U^*_{\alpha i} U_{\beta i} e^{-i m_i^2 \frac{L}{2E}} \right|^2 \tag{2.8}$$

This equation can be rewritten by using trigonometric functions and separating the real and imaginary parts:

$$P(\alpha \to \beta) = \delta_{\alpha\beta} - 4 \sum_{i>j} \mathrm{Re}(U^*_{\alpha i} U_{\beta i} U_{\alpha j} U^*_{\beta j}) \sin^2\left(\frac{\Delta m^2_{ij} L}{2E}\right) + 2 \sum_{i>j} \mathrm{Im}(U^*_{\alpha i} U_{\beta i} U_{\alpha j} U^*_{\beta j}) \sin\left(\frac{\Delta m^2_{ij} L}{2E}\right) \tag{2.9}$$

where $\Delta m^2_{ij} = m^2_i - m^2_j$ are the mass-squared differences. In the case of three-flavor oscillation, there are three mass-squared differences of which two are independent. Experiments have shown that one mass-squared difference is about two magnitudes larger than the other. The larger one is usually called $(\Delta m^2)_{atm}$ and the smaller one $(\Delta m^2)_{sol}$, referring to the respective solar or atmospheric origin of the detected neutrinos. However, the actual hierarchy (ordering) of the mass differences is still unknown and can be either the normal mass hierarchy (NH) or the inverted mass hierarchy (IH) (see figure 2.1).

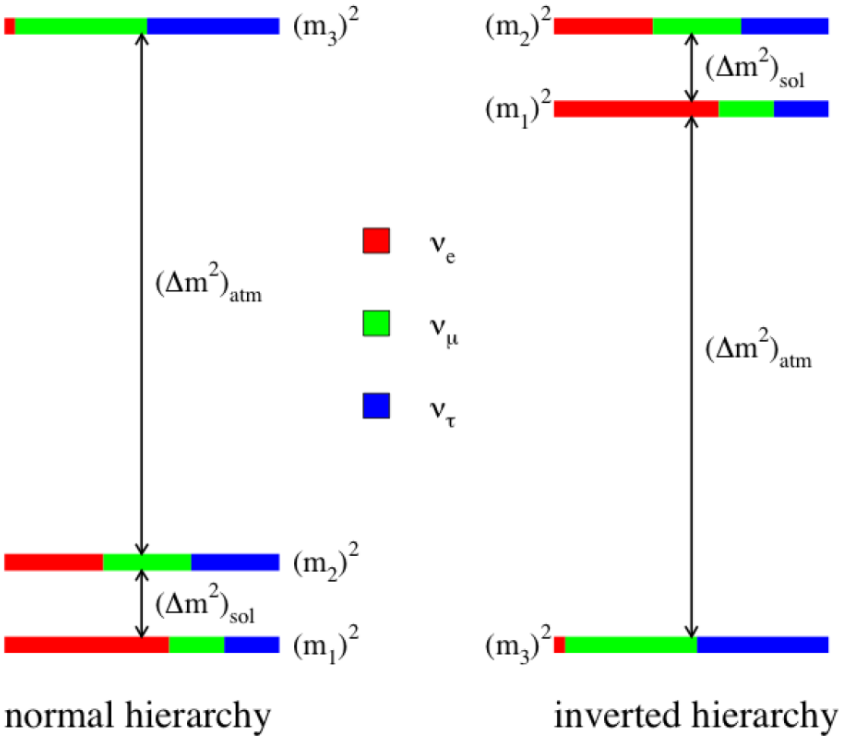

Figure 2.1: Ordering of neutrino mass eigenstates in the normal hierarchy (left) and the inverted hierarchy (right). The colors depict the contribution of the neutrino flavor eigenstates to each mass eigenstate.

Two-flavor case

In case of just two neutrino flavors, the mixing matrix simplifies to a two-dimensional rotation matrix that only depends on one mixing angle θ as parameter:

$$U = \begin{pmatrix} \cos\theta & \sin\theta \\ -\sin\theta & \cos\theta \end{pmatrix} \tag{2.10}$$

With only two neutrino flavors, there is a single mass-squared difference $\Delta m^2 = m_2^2 - m_1^2$. Using equation 2.8 the oscillation probability can be calculated as:

$$P(\alpha \to \beta) = \left| -\sin\theta\cos\theta e^{-im_1^2\frac{L}{2E}} + \cos\theta\sin\theta e^{-im_2^2\frac{L}{2E}} \right|^2 \tag{2.11}$$

$$= \sin^2\theta\cos^2\theta \left[2 - \cos\frac{(m_2^2 - m_1^2)L}{2E} \right] \tag{2.12}$$

$$= \sin^2(2\theta)\sin^2\left(\frac{\Delta m^2 L}{4E}\right) \tag{2.13}$$

Mixing parameters

The measurement of the mixing angles and the mass-squared differences has been the focus of several experiments. The oscillation probability depends on more than one parameter and at present it is not possible for one experiment to measure the full set of mixing parameters. One specific experiment is usually designed such, that some mixing parameters are negligible in the analysis. Assuming normal mass hierarchy, the results from various neutrino oscillation experiments have been analyzed and the best fit values at 1σ confidence level (CL) are presented in table 2.3.

Mixing parameter	**best fit**	**1σ range**
Δm^2_{21} $[10^{-5}\,\mathrm{eV}^2]$	7.62	7.43-7.81
$\lvert\Delta m^2_{31}\rvert$ $[10^{-5}\,\mathrm{eV}^2]$	2.55	2.46-2.61
$\sin^2\theta_{12}$	0.320	0.303-0.336
$\sin^2\theta_{23}$	0.613 (0.427)	0.400-0.461 (0.573-0.635)
$\sin^2\theta_{13}$	0.0246	0.019-0.030
δ_{CP}	0.80 π	0-2π

Table 2.3: Neutrino oscillation parameters of a fit to global data [13] made in 2012. The $\sin^2\theta_{23}$ value given in brackets is the local minimum in the first octant of θ_{23} with $\Delta\chi^2 = 0.02$ with respect to the global minimum.

2.2.2 Neutrino oscillations in matter

If neutrinos propagate through matter, the behavior of neutrino oscillations changes due to the weak interactions with the constituents of matter. In 1978 Lincoln Wolfenstein realized that coherent forward scattering has to be considered for neutrino oscillations

in matter [14]. The resulting modifications on neutrino oscillations in comparison to the vacuum case, are explained in this section.

Neutrino interactions in matter mostly occur with first-generation leptons and quarks. The main effect represents the coherent forward scattering of neutrinos. Coherent forward scattering is possible via neutral current (NC) reactions with leptons and quarks and charged current (CC) reactions with leptons. One can neglect the NC reactions because they only lead to a flavor-independent effect, which has no impact on the oscillation probabilities. As ordinary matter consists only of protons, neutrons and electrons, this leaves only one CC reaction between ν_e and electrons. Thus, neutrino propagation through matter differentiates between the electron neutrino and the other neutrino flavors because of the additional CC contribution. The resulting extra potential can be written as:

$$V_{\nu_e} = \sqrt{2} G_F n_e \tag{2.14}$$

where n_e is the electron density and G_F the Fermi coupling constant. Another, more practical, notation is

$$V_{\nu_e} = 7.56 \cdot 10^{-14} \left(\frac{\rho}{g/cm^3} \right) Y_e \,\mathrm{eV} \tag{2.15}$$

with the matter density ρ and Y_e denoting the number of electrons per nucleon, which is 0.5 in an electrically neutral isoscalar medium. This potential has to be added to the total Hamiltonian. With $A = V_{\nu_e} E$, where E is a matrix with $E_{\nu_e,\nu_e} = 1$ and all other elements equal to zero, the total Hamiltonian is:

$$H = U \frac{m^2}{2E} U^\dagger + A \tag{2.16}$$

Two-flavor case

If a constant electron number density $n_e(\vec{r}, t) = n_e$ is considered, the interaction Hamiltonian becomes time-independent and the oscillation probability can be derived similarly to the vacuum case. A detailed description can be found in [9]. To describe oscillation in matter by the same equations as in the vacuum case, the two replacements, $\Delta m^2 \to \Delta m^2_m$ and $\theta \to \theta_m$, are necessary:

$$\Delta m^2_m = \Delta m^2 \sqrt{\sin^2(2\theta) + \left(\cos(2\theta) - \frac{A}{\Delta m^2} \right)^2} \tag{2.17}$$

$$\sin^2 2\theta_m = \frac{\sin^2 2\theta}{\sin^2(2\theta) + \left(\cos(2\theta) - \frac{A}{\Delta m^2} \right)^2} \tag{2.18}$$

With these definitions of the matter oscillation parameters, the oscillation probability now has the same form as in the vacuum case. In the case of $A = 0$, the oscillation probability

equals the vacuum oscillation probability.

$$P_m(\alpha \to \beta) = \sin^2(2\theta_m) \sin^2\left(\frac{\Delta m_m^2 L}{4E}\right) \tag{2.19}$$

Neutrino oscillations in matter give rise to several phenomena that do not occur in vacuum. One of these is the MSW[3] effect, which describes a resonance of maximal mixing in matter [15]. The necessary condition is satisfied if $A = \Delta m^2 \cos(2\theta)$ whereby equation 2.19 becomes maximal.

[3]MSW: Mikheyev-Smirnov-Wolfenstein

Chapter 3

Core-collapse supernovae

The explosion of a supernova is one of the most energetic events in the universe. It occurs as the final step in the lifetime of massive stars. It is known today that there are two different classes of supernovae. The analysis conducted in the scope of this thesis is based on the class of "core-collapse supernova" (SN). The necessary condition for a SN is a massive star with approximately $8\,M_\odot$[1] or more. The remnant of a SN forms a neutron star (NS) if the initial mass is below $\sim 25\,M_\odot$, while above this mass the remnant forms a black hole (BH). A detailed SN model will be discussed in section 3.1. Furthermore, there are "thermonuclear supernovae", which most likely happen in a binary star system with a white dwarf. In the explosion, the white dwarf is completely disrupted. An overview of models of this class of supernovae can be found in [16].

Historically, supernovae have been divided into two categories: Supernovae with spectral lines from hydrogen are classified as type I (subtypes: a, b, c), while supernovae without spectral lines from hydrogen are classified as type II (subtypes: L, P). However, this classification does not coincide with the two types mentioned before. In fact, only the subtype Ia refers to a thermonuclear supernova.

From the observations of other galaxies, we expect roughly 1-3 SNe per century in our galaxy. About 99 % of their energy is released in the form of neutrinos, which make SNe very likely to be the most intense astronomical neutrino sources. Neutrinos from a progenitor star with a mass of $8\,M_\odot$ are expected to carry away about $3{\cdot}10^{53}\,\mathrm{erg}$ ($3{\cdot}10^{46}\,\mathrm{J}$) in about 10 seconds. In general, neutrinos play an important role in SN models, and section 3.2 will analyze the expected neutrino signal.

Neutrino astronomy has been promoted with the detection of neutrinos from the supernova SN1987A. Although only a handful neutrinos were detected, this signal already contributed greatly to the understanding of SN physics, and some of the results will be reviewed in section 3.3. However, the detailed explosion mechanism is still unknown and a high-statistics signal would be significantly more helpful. Furthermore, the neutrinos from a SN allow to study intrinsic neutrino properties, such as giving constraints on neu-

[1] $1\,M_\odot$: 1 solar mass, $\sim 2{\cdot}10^{30}\,\mathrm{kg}$

trino the mass hierarchy, neutrino velocity and mixing parameters. Moreover, one should keep in mind that SNe are responsible for the enrichment of heavy elements in our galaxy and therefore played a crucial role in the development of life.

3.1 Standard core-collapse supernova model

A star releases energy by the nuclear fusion of elements. Over time, the star goes through several stages of element burning: The sequence starts with the fusion of hydrogen to helium. The released energy heats the core and creates pressure, preventing a gravitational collapse. Eventually, the hydrogen is exhausted and the nuclear fusion slows down. This leads to a contraction of the star, whereupon the temperature and the pressure in the core start to rise. At a certain point, the temperature is high enough to allow fusion of helium to carbon in the so-called triple-alpha process. In this process, three Helium-4 nuclei are fused to carbon. Massive stars repeat this procedure several times and thus reach further stages of element burning. Namely, they go through the stages of carbon-, neon-, oxygen- and finally silicon-burning. In the last step, silicon is mainly fused to the radioactive ^{56}Ni, which has a half-life of 6.1 days and decays into ^{56}Co with a half-life of 77.1 days. Subsequently, the ^{56}Co decays into the stable ^{56}Fe.

Iron has the highest binding energy per nucleon of all elements and therefore cannot release energy by nuclear fusion or fission. This sequence is the reason why massive stars develop a so-called "onion-skin" structure just before they explode: The core consists of iron and is surrounded by shells of lighter elements. This structure is assumed to be the initial situation for the explosion of a core-collapse supernova. This description of the model is mainly based on [11] and [17].

Initial phase of collapse

While more and more iron is produced, the core mass density increases. During this period, it is the pressure of the degenerate relativistic electron gas in the iron which prevents the star from gravitational collapse. As soon as the mass of the core exceeds about $1.4\,\mathrm{M}_\odot$, known as the Chandrasekhar limit, the degeneracy pressure cannot prevent the collapse anymore. At this point, the mass density of the core has reached $\rho \sim 10^{10}\,\mathrm{g\,cm^{-3}}$ with a temperature of about $T \sim 10^{10}\,\mathrm{K}$, whereupon electron capture on iron occurs:

$$^{56}\mathrm{Fe} + e^- \rightarrow {}^{56}\mathrm{Mn} + \nu_e \tag{3.1}$$

This leads to a reduction of the electron gas pressure and the core loses energy through neutrino emission. Additionally, endothermic photodissociation of iron nuclei takes place:

$$^{56}\mathrm{Fe} + \gamma \rightarrow 13\alpha + 4n - 124.4\,\mathrm{MeV} \tag{3.2}$$

This process exhausts the internal energy of the core contraction and therefore reduces the thermal pressure support. Both effects contribute to an accelerated collapse of the core.

Neutrino trapping

As the core proceeds to contract, the core mass density reaches 10^{11} - $10^{12}\,\mathrm{g\,cm^{-3}}$ and neutrinos become trapped in the core. At this point, the neutrinos mean free path becomes smaller than the size of the iron core. They propagate diffusely because of coherent elastic scattering on heavy nuclei. Neutrinos in the core are in thermal equilibrium in a degenerate Fermi sea. One can define a so-called "neutrino sphere" in analogy to the photosphere of the sun. As the mass density decreases with increasing radius, only neutrinos outside the neutrino sphere can move freely. The exact position of the neutrino sphere is flavor-dependent, which results from different opacities (see below) for the different flavors.

Bounce and shock propagation

The collapsing core consists of two parts with different infall velocities. The inner core is collapsing at subsonic velocities, where the speed proportional to the radius (homologous collapse), while the outer core falls in supersonically. When the core density rises above the order of $10^{14}\,\mathrm{g\,cm^{-3}}$, nuclear densities are reached. The repulsive nuclear forces quickly bring the collapse to a stop, but this does not propagate beyond the point where the speed of sound equals the infall velocity. Therefore, material keeps falling in from the outer core and gets reflected, building up a shock wave. This process is often referred to as the "bounce". As more material falls in and stores energy into the shock wave, the shock wave begins to move outwards. Core bounce and shock wave formation can be seen as the starting point that ultimately triggers a supernova explosion. But it also triggers growing uncertainties of the exact explosion mechanism. Current SN models suggest that the shock wave may not have enough energy to reach the outer layers [18]. On the propagation into the outer core, the shock wave dissociates nuclei into free nucleons, losing about 8.8 MeV per nucleon. Subsequently, the process of electron capture takes place in the region behind the outward-moving shock front, which produces a huge number of ν_e:

$$e^- + p \rightarrow n + \nu_e \tag{3.3}$$

As the shock passes the neutrino sphere, the formerly trapped electron neutrinos can now escape in less than 20 ms. During this short time span, roughly 1 % of the total binding energy is emitted. This is often referred to as the "prompt ν_e burst" or "prompt deleptonization burst". The prompt ν_e burst takes place almost at the same time as the appearance of the other neutrino flavors. These are produced in the hot post-bounce region where several reactions take place. Thermally produced positrons lead to the

production of $\bar{\nu}_e$ via:

$$e^+ + n \rightarrow p + \bar{\nu}_e \tag{3.4}$$

The production of $\nu_{\mu,\tau}$ and $\bar{\nu}_{\mu,\tau}$ occurs in processes where all neutrino flavors are created. These processes are electron-positron annihilation:

$$e^+e^- \rightarrow \nu\,\bar{\nu} \tag{3.5}$$

$\nu_e\bar{\nu}_e$ annihilation:

$$\nu_e\,\bar{\nu}_e \rightarrow \nu\,\bar{\nu} \tag{3.6}$$

as well as nucleon-nucleon bremsstrahlung:

$$NN' \rightarrow NN' + \nu\,\bar{\nu} \tag{3.7}$$

Accretion phase and delayed explosion

At a radial distance of $100 - 200\,\mathrm{km}$, the shock finally stalls as a result of the described energy loss. The newly-born "proto-neutron star" (PNS) has a radius of $50 - 80\,\mathrm{km}$. Matter keeps falling in and releases gravitational energy. The hot and dense core still produces high-energy neutrinos of all flavors. A model to explain the final break-out is energy the transfer from neutrinos to material close to the stalled shock. If this energy transfer is large enough, it can revive the shock, leading to the delayed but final explosion. This process requires several hundreds of milliseconds.

Cooling phase and nucleosynthesis

Cooling of the neutron-star proceeds through the diffusive emission of neutrinos. The time scale of this process is supposed to be about several seconds. Nucleosynthesis leads to the production of heavy nucleon-rich elements. The rapid neutron capturing (r-process) may take place in the region between the proto-neutron star and the escaping shock wave, sometimes called "hot bubble". However, there are lots of uncertainties in the details of the r-process in SN.

3.2 Core-collapse supernova neutrino signal

This section will focus on the expected neutrino signal from a SN. This description mainly follows [17] and [19]. Neutrinos allow to look deep inside the SN, which is not possible with electromagnetic waves, because of photon scattering. As already indicated in the last section, the production of neutrinos is closely related to the dynamics and the physical state of a SN. Before looking into the details of the neutrino signal, one can start to study the overall features. This analysis will focus on the case where the remnant of the SN forms a neutron star. The entire energy release of a SN is roughly the same as the binding

energy of the neutron star:

$$\Delta E \approx \frac{3}{5}\frac{G_N M_{NS}^2}{R_{NS}} = 1.60 \cdot 10^{53}\,\mathrm{erg}\left(\frac{M}{M_\odot}\right)^2\left(\frac{10\,\mathrm{km}}{R}\right) \tag{3.8}$$

As already mentioned earlier, about 99% of the energy is released via neutrino emission. One has to keep in mind that the observed energies can be significantly changed for a distant viewer due to gravitational redshift. The average energy of the thermal neutrinos can be estimated by applying the virial theorem: It states that the average kinetic energy of a nucleon near the neutron star surface must be half of its gravitational potential, giving $2\langle E_{kin}\rangle \approx \frac{G_N M M_n}{R}$. In a typical case of a neutron star ($\mathrm{M} = 1.4\,\mathrm{M}_\odot$, $\mathrm{R} = 15\,\mathrm{km}$), this implies neutrino energies of several tens of MeV. The whole energy is distributed equally between the six different neutrino species.

The expected supernova signal is usually split into ν_e, $\bar{\nu}_e$ and ν_x signals, where ν_x denotes the flavors of $\nu_{\mu,\tau}$ and $\bar{\nu}_{\mu,\tau}$. Classic SN models suggest different average energies and spectra for the different flavors. This is caused by the fact that the radius of the neutrino sphere, where neutrinos decouple from matter, is flavor-dependent. This flavor dependency of the neutrino sphere originates from different opacities for the neutrino flavors. For electron flavor neutrinos, the dominant sources of opacity are the charged current reactions $\nu_e + n \rightarrow p + e^-$ and $\bar{\nu}_e + p \rightarrow n + e^+$ respectively. In contrast, the dominant sources of opacity for ν_x are elastic neutral current scattering reactions. There are no charged current reactions, as the energies of the ν_x are too small to produce large-mass μ and τ leptons. This is the reason for the ν_x to decouple closer to the core at higher mass density and temperature, and therefore carry more energy than the electron flavor neutrinos. Furthermore, there is a difference between the two electron flavors: The ν_e decouple at a larger radius because the number of neutrons is higher than the number of protons which leads to a higher interaction rate. Hence, the resulting neutrino signal has the following energy hierarchy: $\langle E_{\nu_e}\rangle < \langle E_{\bar{\nu}_e}\rangle < \langle E_{\nu_x}\rangle$. As the total energy is split up equally between the neutrino flavors, the neutrino flux is anti-proportional to the average energy.

Recent studies suggest that the differences between the average energies are not very strong. In these more complex studies, the decoupling from matter for the ν_x is described as a two-step process. The ν_x decouple at the so-called “energy sphere” and then enter the “scattering atmosphere”. The neutrino-nucleon cross section depends on the squared neutrino energy, making the energy spectrum skewed to lower energies in analogy to a ”low-pass filter”. The resulting mean energy of the ν_x can be as low as 60% of the original energy mean energy of the energy sphere. Therefore, the ν_x spectrum might be very similar to the spectrum of the electron flavors. The decoupling of electron flavor neutrinos and the other flavors is illustrated in figure 3.1

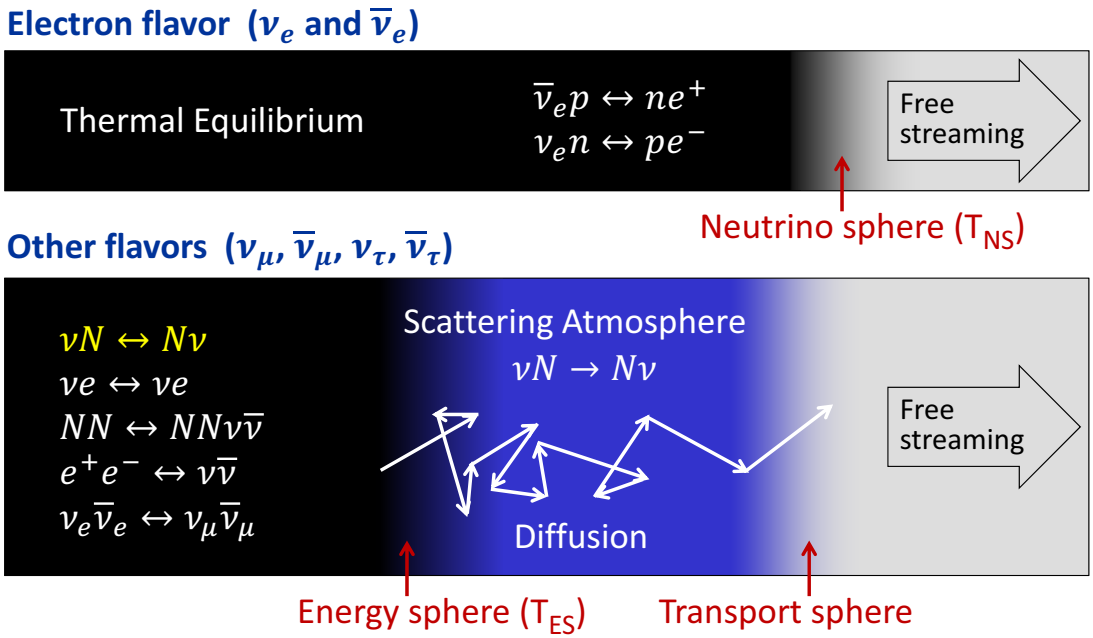

Figure 3.1: Neutrino decoupling from matter in a core-collapse supernova for electron flavor neutrinos (top) and the other flavors (bottom) [19].

The interactions between matter and neutrinos are sufficient to realize thermal equilibrium. Therefore, the energy distribution of the emitted neutrinos can be described by a Fermi-Dirac spectrum. One has to keep in mind that the cross sections for the neutrino interactions are energy-dependent. The interaction rate of neutrinos with lower energies is less than it is for high-energy neutrinos wherefore their neutrino spheres have smaller radii. Hence, the energy spectrum has a "pinched" form compared to a Fermi-Dirac distribution. A common parametrization of the time-integrated flux respectively fluence for the respective neutrino flavor ν_α is the so-called "pinched Fermi-Dirac" spectrum:

$$F^0_\alpha(E) = \frac{1}{F(\eta_\alpha)} \frac{L_\alpha}{T^4_\alpha} \frac{E^2}{e^{E/T_\alpha - \eta_\alpha} + 1} \tag{3.9}$$

where $F(\eta_\alpha)$ is a normalization factor, T_α is the effective neutrino temperature, L_α is the number luminosity and η_α a dimensionless pinching parameter.
The neutrino signal can be divided into three characteristic phases reflecting the phases of the explosion model. Figure 3.2 illustrates how the luminosities and the average energies for the different flavors vary in each phase. More recent studies confirm this picture but suggest that the so far assumed energies of the ν_x are probably 1-2 MeV too high [19].

1. **Prompt ν_e burst.** The first phase includes the time from the bounce up to a few tens of milliseconds. The neutrino signal is dominated by the neutronisation burst, which lasts only for about 20 ms. The neutrinos cannot escape until they reach the neutrino sphere. The average energy of the ν_e reaches its maximum of about 15 MeV. Simultaneously, the production of $\bar{\nu}_e$ and ν_x begins.

2. **Accretion phase.** The time span of the accretion phase typically covers a few hundred ms. In this period, the average energies and luminosities of the $\bar{\nu}_e$ and ν_x rise due to the increasing temperature of the region where the neutrinos are emitted. The ν_x are emitted closer to the SN core, which is why their energies are higher than those of the other flavors. However, their flux is smaller. The specific neutrino signal is affected by the mass profile of the accreted matter [17].

3. **Cooling phase.** During the cooling phase of the proto-neutron star, the neutrino luminosities are decreasing roughly exponentially over time. The luminosities of the neutrino flavors do not differ very much. The average ν_e energy is slightly lower than that of the other flavors.

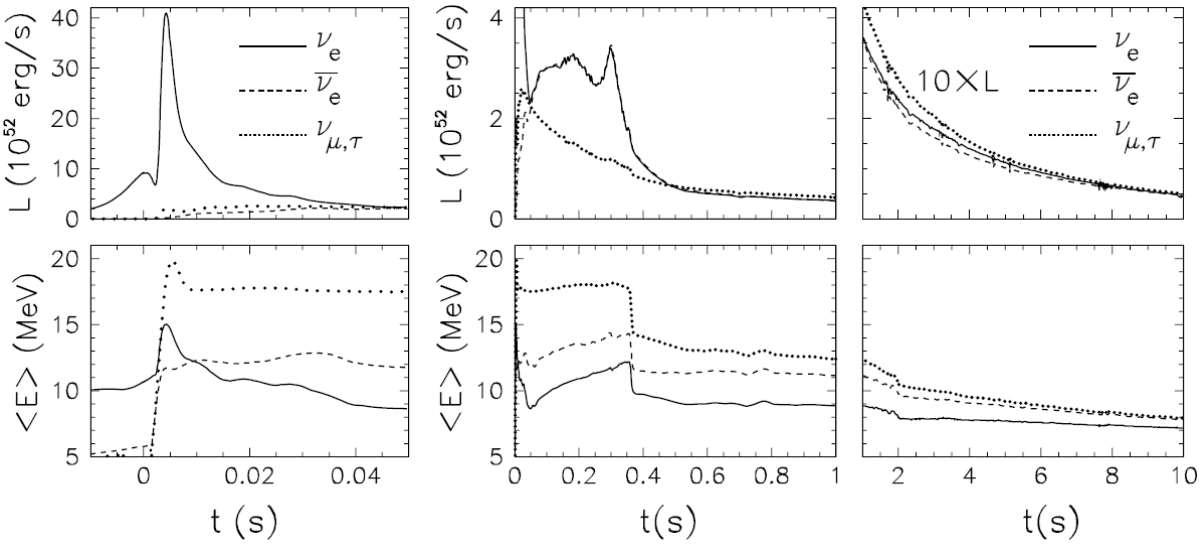

Figure 3.2: Neutrino luminosities (top row) and mean energies (bottom row) with respect to the time after bounce for a $10.8\,M_\odot$ progenitor according to a numerical simulation of the Basel group [20]. All quantities are in the laboratory frame of a distant observer. Left: Prompt ν_e burst. Middle: Accretion phase. Right: Cooling phase.

3.3 Signal of SN1987A

This section will summarize the neutrino signal and the results of the analysis of SN1987A and is mainly based on [19]. The observation of neutrinos from the SN1987A has been a historic breakthrough for neutrino astronomy. The SN was observed on 23rd February 1987 in the Large Magellanic Cloud at a distance of about 51.4 kpc (168,000 light-years) from earth. Three separate neutrino detectors have simultaneously (within their time uncertainties) observed an overall number of 24 events. Two water Cherenkov detectors, the Kamiokande and the Irvine-Michigan-Brookhaven (IMB) experiments detected 11 and 8 antineutrinos. The Baksan Scintillator Telescope (BST) observed 5 antineutrinos. The

total burst lasted less than 13 seconds. All neutrinos were observed roughly three hours before the optical brightening. Figure 3.3 displays the energy of the observed events. The Liquid Scintillator Detector (LSD) observed a 5-event cluster a few hours prior to the other neutrino events. Since there was no other simultaneous signal, this is not considered to be associated with SN1987A.

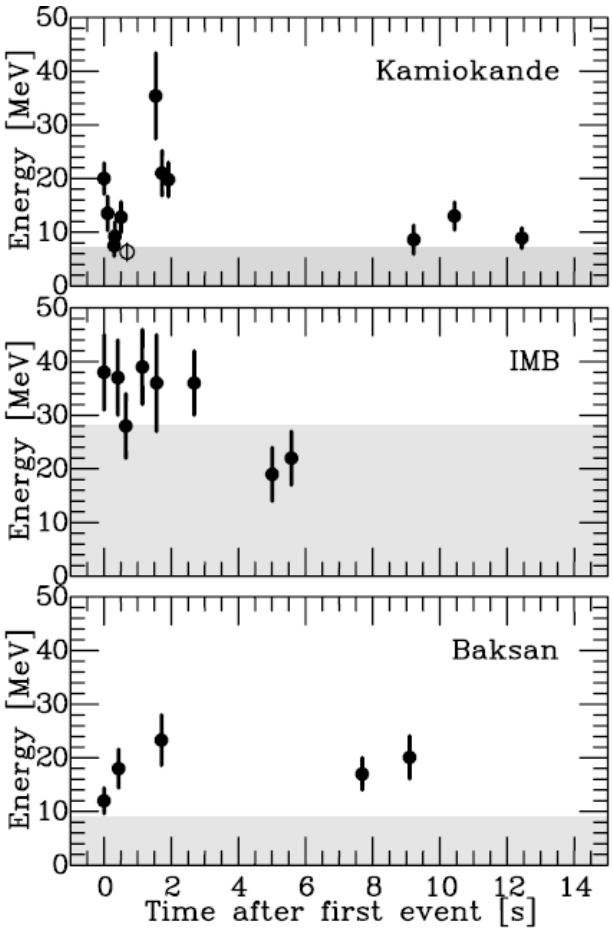

Figure 3.3: The neutrino events of SN1987A at Kamiokande, IMB and Baksan. The shaded area corresponds to trigger efficiencies of less than 30 %. The specially marked event in the Kamiokande plot is considered as background. The respective first event for each detector has been shifted to t = 0. [19]

Over the years, the neutrino signal of SN1987A has been analyzed in various ways. Overall, the observed events could confirm the general picture of the core-collapse SN model. The duration of the neutrino signal is 12.4 s in Kamiokande and 5.6 s in IMB, which is consistent with the expected order of about 10 seconds. Moreover, the measured energy distribution agrees with the expected thermal emission. The average energy of the time-integrated flux of $\bar{\nu}_e$ was calculated to be about 9 MeV [19].

Chapter 4

The LENA experiment

The 50 kt liquid scintillator detector LENA[1] is one of three detector options proposed within the European LAGUNA[2] project. This project aims to study the feasibility of a next generation neutrino observatory, which would offer new scientific opportunities in the field of particle and astroparticle physics. In particular, the project addresses studies on neutrino properties, astrophysical and terrestrial neutrino sources and the radioactive decay of protons. Besides the LENA detector, the water Cherenkov detector MEMPHYS[3] and the liquid argon detector GLACIER[4] are under investigation within the LAGUNA project.

LENA is an experiment which combines the size of a detector like Super-Kamiokande [1] with the scintillator detection principle of experiments like Borexino [2] or KamLAND [3]. Some characteristics of the scintillator technique are high energy resolution below 10 MeV, a low detection threshold ($\sim$200 keV) as well as an excellent background discrimination. The size of LENA enables high-statistics measurements of strong neutrino sources like core-collapse supernovae, the Sun or the Earth's interior, which will resolve energy spectra and their time evolution. LENA is a multi-purpose detector and an overview of the broad physics program is given in section 4.2. Beforehand, the design of LENA and its key components are discussed in section 4.1. This chapter is based on the LENA whitepaper [21].

4.1 Detector design

This section starts with an overview of the detector and then focuses on some important detector components in more detail. A schematic drawing of the detector can be seen in figure 4.1. The target mass of 50 kt liquid scintillator is planned to be hold in an

[1]Low Energy Neutrino Astronomy
[2]Large Apparatus for Grand Unification and Neutrino Astrophysics
[3]MEMPHYS: Megaton Mass Physics
[4]GLACIER: Giant Liquid Argon Charge Imaging Experiment

unsegmented tank consisting of concrete. Because of experimental advantages a radial-symmetric design is foreseen. The dimensions of the tank are 100 meter in height and 32 meter in diameter and the wall thickness is six meter. The scintillation light is detected by photomultiplier tubes (PMTs) which are carried at a distance of one meter from the tank wall by the PMT support structure (PSS). Shielding from cosmic background like muons is crucial, thus the whole detector is placed in a cavern in an underground laboratory. The currently favoured site is the Pyhäsalmi mine in Finland, which already hosts a small underground laboratory, the Finnish Center for Underground Physics in Pyhäsalmi (CUPP). The interspace between the cavern walls and the tank is filled with water and equipped with 2000 PMTs. This outside water volume is used as shielding as well as an active Cherenkov veto against muons. For the top muon veto several options are under discussion, like plastic scintillator panels, limited streamer tubes or resistive plate chambers. On top of the whole detector is space for data acquisition (DAQ) and technical facilities.

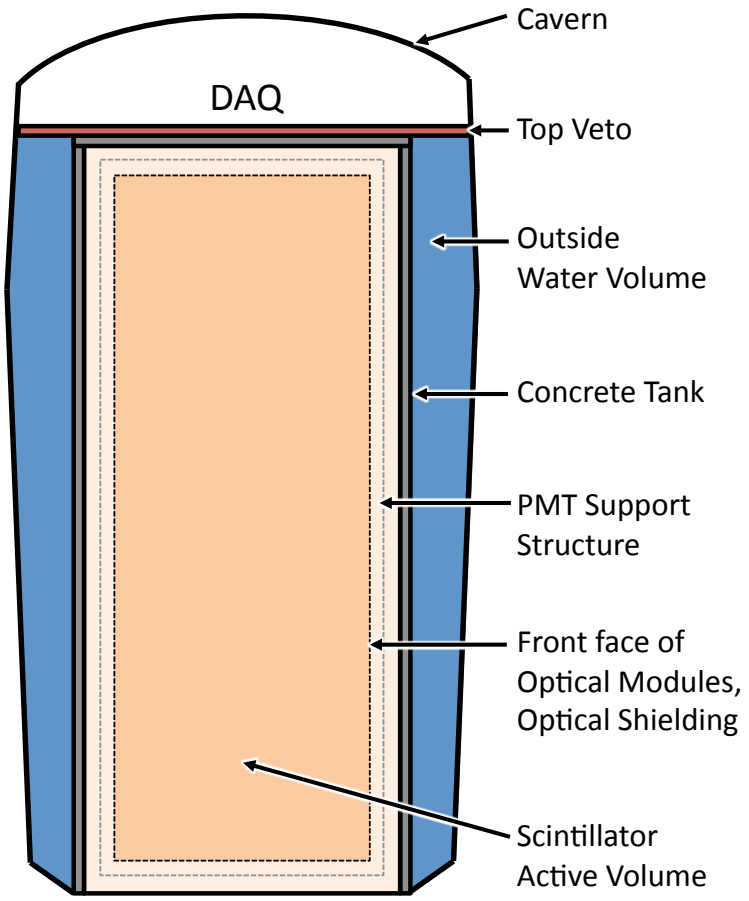

Figure 4.1: Schematic drawing of the LENA tank and cavern

4.1.1 Liquid scintillator

The detection of a particle in liquid scintillator is based on electromagnetic interactions between the particle and the scintillation molecules. Since neutrinos only interact via weak interactions, they can only be detected if they produce charged particles in previous weak interactions. The detection channels for SN neutrinos in LENA can be found here 5.1. Following, the the detection principle of charged particles in liquid scintillator is described.

When a charged particle propagates through liquid scintillator it excites or ionizes electrons of the scintillation molecules along its path. Their subsequent deexcitation produces photons in the near UV which are emitted isotropically. For heavy charged particles, e.g. protons or alpha particles, the energy deposition per unit length dE/dx can be approximated by the Bethe formula [22]. However, there are several processes, for instance radiationless deexcitation, reducing the efficiency of light to energy conversion, which are summarized in the term "quenching". Due to quenching the dependence of the energy deposition per unit length dE/dx and the number of emitted scintillation photons per unit length dL/dx is in general not linear. Nevertheless, dL/dx can be approximated by the semi-empirical formula called Birks' law:

$$\frac{dL}{dx} = L_0 \frac{\frac{dE}{dx}}{1 + k_B \frac{dE}{dx}} \tag{4.1}$$

where k_B denotes the material dependent Birks constant and L_0 denotes a normalization constant.

As several molecular deexcitation modes are possible, the shape of the resulting scintillation pulse can be described as the sum of exponential decay functions:

$$n(t) = \sum_i n_i \, e^{-\frac{t}{\tau_i}} \tag{4.2}$$

where τ_i denotes the decay time constant of the corresponding decay process and n_i its amplitude. The amplitudes of the decay processes depend on dE/dx, which on the other hand depend on the type of particle. Therefore, the pulse shape can be used for particle discrimination of alpha particles or protons from electrons. Emission and absorption spectra of a single-component scintillator has a significant overlap. In order to shift the scintillation light to a longer wavelength, usually solutes (so-called wavelength shifter) are added to the liquid scintillator. Hence, the scintillator becomes transparent to the wavelength shifted scintillation light, which prevents multiple absorption and reemission processes and thus a lost of timing and energy information.

The most promising liquid scintillator under consideration is LAB[5] ($C_{18}H_{30}$) but also PXE[6] ($C_{16}H_{18}$) is under discussion. Some parameters of chemical and optical properties can be found in table 4.1. LAB is superior regarding the numer of free protons, attenuation length and scattering length, whereas PXE has the advantage to be faster, because of a smaller decay time constant. With PPO[7] and Bis-MSB[8] there are two candidate solutes under investigation, which can be added as wavelength shifters. Some parameters can be found in table 4.2.

Solvent	**LAB**	**PXE**
Chemical formula	$C_{18}H_{30}$	$C_{16}H_{18}$
Molecular weight [g/mol]	241	210
Density ρ [kg/ℓ]	0.863	0.986
Flash point [°C]	140	167
Molecular density [10^{27}/m^3]	2.2	2.8
Free protons [10^{28}/m^3]	6.6	4.7
Carbon nuclei [10^{28}/m^3]	4.0	4.2
Total p/e$^-$ [10^{29}/m^3]	3.0	3.2
Refractive index n	1.49	1.57
Absorption maximum [nm]	260	270
Emission maximum [nm]	283	290
Attenuation length L [m]	$\sim$20	12
Scattering length ℓ_s [m]	25	22

Table 4.1: Some chemical and optical properties of PXE and LAB. This table is taken from the LENA whitepaper [21].

Solute	**PPO**	**Bis-MSB**
Chemical formula	$C_{15}H_{11}NO$	$C_{24}H_{22}$
Absorption maximum	303 nm	345 nm
Emission maximum	365 nm	420 nm

Table 4.2: Some properties of the solutes PPO (2,5-diphenyl-oxazole) and Bis-MSB (1,4-bis-o-methylstyryl-benzene). This table is taken from the LENA whitepaper [21].

[5]Linear Alkylbenzene
[6]Phenyl-o-xylylethane
[7]Diphenyloxazole
[8]Bismethylstyrylbenzene

4.1.2 Optical modules

The current choice of photosensors are bialkali PMTs. They are part of the optical module which can be seen in figure 4.2. The optical module (OM) includes an electronics socket at the PMT base with a liquid-tight connector on the back for high voltage and signal cables. The whole OM is encapsulated with steel against pressure with a curved acrylic window closing the cone aperture in front of the PMT. Furthermore, a light-concentrating mirror (so-called Winston cone) is mounted in front of the PMT and a mineral oil buffer is enclosed inside the Winston cone. Finally, a mu-metal at the inner surface of the encapsulation is shielding the PMT from external electromagnetic fields.

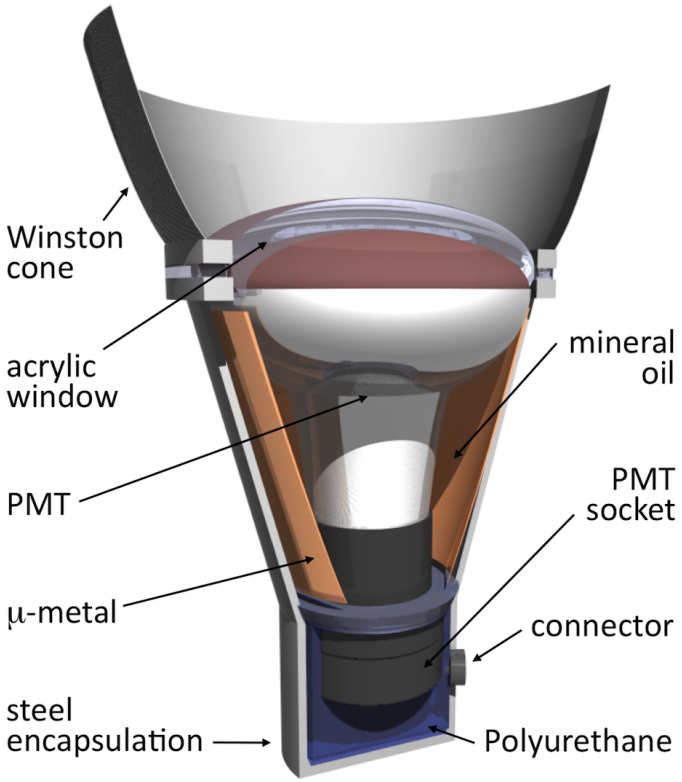

Figure 4.2: Illustration of an optical module in LENA [21]

The PMTs translate the scintillation photons to photo electrons, which subsequently are amplified into a measurable signal. It is foreseen to use FADCs[9] to readout the full pulse shape information of each individual PMT. The aimed optical coverage, i.e. the fraction of the detector's surface covered by photosensors, is 30%. This value can be reached with either 73000 8-inch or 32000 12-inch PMTs, with the latter being the default option. Both options correspond to an optical coverage of 22%, which can be increased to 35% if parabolic Winston cones are mounted on top of the PMTs. Along with the optical coverage the photo detection efficiency determines the overall light detection efficiency in LENA. The baseline value for the photo detection efficiency is assumed to be 20% at 420 nm, which is a conservative assumption for current PMTs.

[9]Fast Analogue-to-Digital Converter

4.2 Physics program

LENA is able to investigate a variety of neutrino sources of different nature. These neutrino sources can be roughly categorized into astrophysical sources (The Sun, SN, DSNB[10]), terrestrial sources (Geoneutrinos, Reactor neutrinos) and high energy sources (Nucleon decay, Long-baseline neutrino beams). This is not a complete list of neutrino sources, but a selection focused on the key aspects of LENA's physics potential. Further research applications, for instance indirect dark matter search or neutrino oscillometry, can be found in the LENA whitepaper [21].
The core science program of LENA is the low-energy regime of neutrino energies up to some tens of MeV. The strong advantages in this energy range originate from the low energy threshold and the good energy resolution. Combined with the large detection volume, LENA is capable to detect astrophysical neutrino sources at large event numbers. Nevertheless, also in the energy regime of hundreds of MeV to some GeV LENA has high physical potential. The following sections give an overview on the variety of research fields that can be addressed with LENA.

4.2.1 SN neutrinos and diffuse supernova neutrino background

Galactic SN are very rare as they only occur a few times per century. Therefore, measuring a high-statistics neutrino signal from a supernova will be a once-in-a-life-time opportunity. LENA provides roughly twice the statistic of Superkamiokande and additionally a superior energy resolution. The golden detection channel for SN neutrinos in LENA is the inverse beta decay. Overall, LENA provides six detection channels, which are discussed in detail in section 5.1. Efficient event discrimination of these detection channels would allow flavor-dependent analysis, which is discussed in chapter 5. The detailed model of SN can be found in section 3.1 and an analysis of the expected neutrino signal in section 3.2.

Another measurement is the signal of the DSNB. This signal originates from the explosion of all past supernovae in the universe. Therefore, an isotropic and constant flux on cosmic scales is expected. However, this flux is very low and can only be measured above 10 MeV, since the reactor neutrino background is too high below 10 MeV. In figure 4.3 the expected DSNB signal based on Maxwell-Boltzmann distribution for different mean energies are shown. The measurement of the average DSNB neutrino energy would provide a possibility to test supernova models.

[10]Diffuse Supernova Neutrino Background

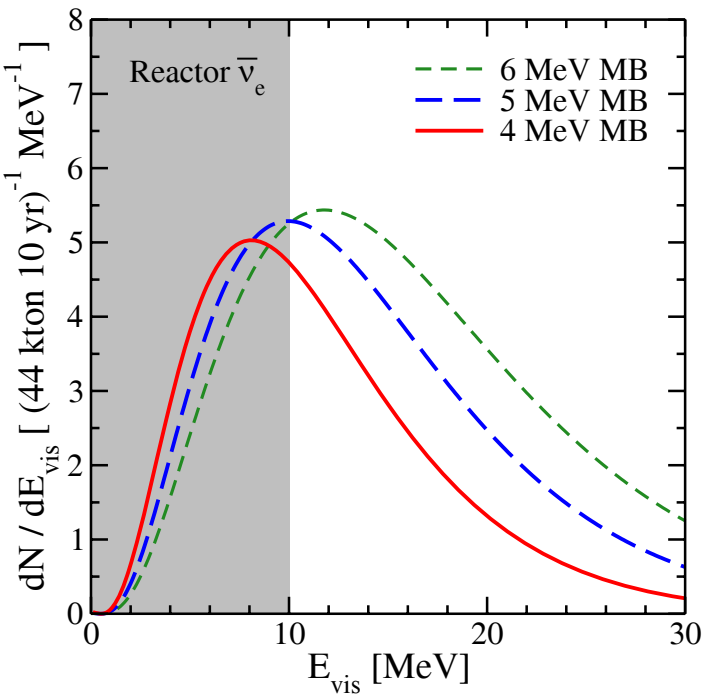

Figure 4.3: Expected DSNB signal spectra based on Maxwell-Boltzmann distribution for three different mean energies as function of visible energy E_{vis}. Below 10 MeV, the reactor neutrino background makes a measurement of the DSNB impossible which is indicated by the grey shading. [21]

4.2.2 Solar neutrinos

The fusion processes in the Sun produce a permanent neutrino flux which can be measured at the Earth. As neutrinos do not heavily interact with solar matter, they escape almost immediately from the Sun. Hence, they do not loose information through multi-scattering and can be used to investigate processes in the deep interior of the Sun. This makes neutrinos valuable for evaluating the Standard Solar Model (SSM), which has been developed since 1963 by John N. Bahcall and others [23, 24]. The SSM prediction of the neutrino spectrum emitted by the Sun is shown in figure 4.4. The two important fusion reactions are the dominant pp-chain[11] and the CNO cycle[12]. Both processes involve several steps.

[11] Proton-Proton fusion reaction
[12] Carbon-nitrogen-oxygen fusion cyle

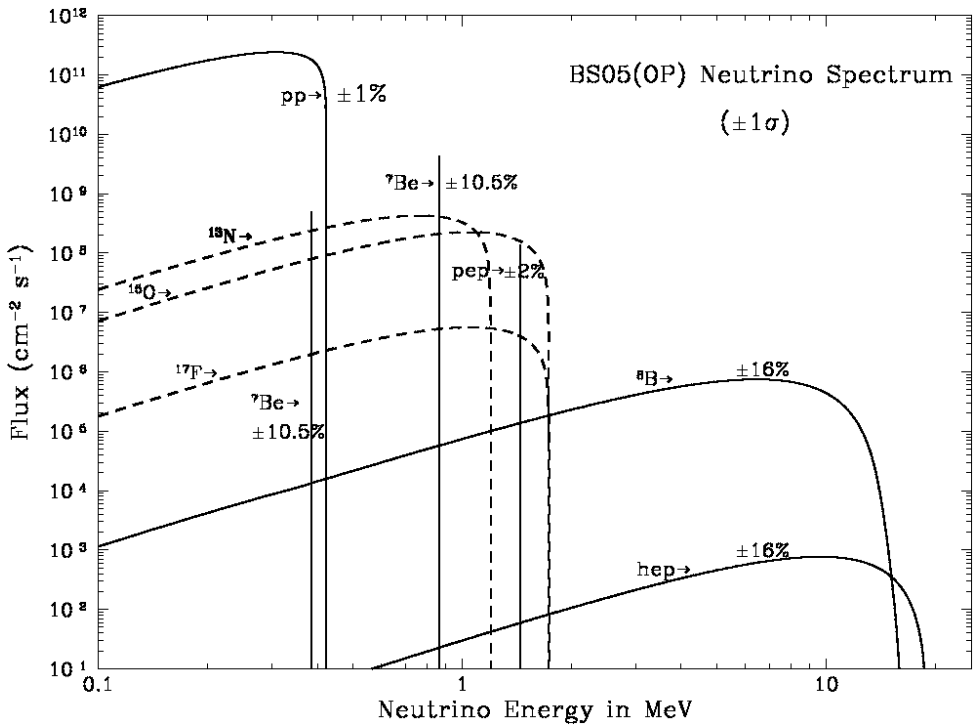

Figure 4.4: Neutrino spectrum emitted by the Sun according to predictions of the SSM [23]. The solid lines indicate neutrinos from the pp-chain while dashed lines indicate the contributions from the CNO-cycle.

As explained previously in section 2.2, the measured deficit of solar neutrinos by Davis contributed strongly to the concept of neutrino oscillation. Since then, it has been identified that solar neutrino oscillations are governed by Δm^2_{12} and θ_{12} of the PMNS mixing matrix. Furthermore, it has been established that at low energies the ν_e survival probability can be described in terms of vacuum oscillations. However, at energies above 1 MeV matter effects lead to an lowered ν_e survival probability, as the oscillation of $\nu_e \rightarrow \nu_{\mu,\tau}$ is enhanced [14, 15]. One possible application of LENA can be the investigation of the vacuum-matter transition region from 1 MeV to about 5 MeV which might reveal some new aspects of neutrino physics. With the high-statistics data resulting from the huge detection volume, LENA would allow a precise determination of SSM neutrino rates and oscillation probabilities.

4.2.3 Geoneutrinos

Geoneutrinos are $\bar{\nu}_e$ produced via beta decays of naturally occurring radio active elements in the Earth. The main contributions originate from ^{40}K and nuclides in the chains of ^{232}Th and ^{238}U. Detection of these low-energy neutrinos is only possible due to a low threshold of liquid scintillator. Measurement of geoneutrinos would allow a determination of abundances and distributions of radioactive elements within our planet. Furthermore, the measurement would help to estimate the amount of these processes to the total heat flux of the Earth constraining geochemical and geophysical models. The main background

to geoneutrinos are neutrinos from nuclear reactors, which are discussed in the next section.

4.2.4 Reactor neutrinos

In nuclear reactors anti-neutrinos are produced by beta decays of fission products. An advantage for analysis of these neutrino is the well known initial energy spectrum. The neutrino signal from nuclear reactors allows a high-statistics measurement of neutrino oscillation effects. In the past there have already been a series of successful experiments measuring reactor neutrinos. It is well established to use the liquid scintillator detection technique in these neutrino reactor experiments. As a result, the most precise measurements of the oscillation parameters Δm^2_{21} and θ_{13} come from reactor neutrino experiments. LENA would be able to diminish the uncertainties especially for the parameter of Δm^2_{21} [21].

4.2.5 Neutrino beam

Although LENA has its outstanding strengths in the low-energy domain it can be used in high-energy applications as well. The LAGUNA project currently investigates a long-baseline neutrino beam for the different detector options. There are several questions which can be addressed with a neutrino beam:

- What is the hierarchy of the neutrino masses (sign of θ_{23})?
- Is the mixing angle θ_{23} maximal?
- Do neutrinos violate the CP symmetry?

LENA would be able to provide one of the most precise measurement of θ_{13} and θ_{23} [21]. A precise measurement of θ_{23} is necessary to understand, if the value of θ_{23} is exactly 45 % corresponding to maximum mixing. Moreover, LENA could measure the sign of $\sin\theta_{23}$, which would determine the mass hierarchy of the neutrino mass eigenstates. The prior goal for these measurements with a neutrino beam is the search for CP-violation. It is currently unknown, if CP-violation is realized in the neutrino sector.

4.2.6 Nucleon decay

LENA offers the opportunity to search for physics beyond the SM with studies on the nucleon decay. Currently, the best limits on proton lifetime come from the Superkamiokande detector [25]:

$$p \to e^+ + \pi^0 \, (\tau > 8.2 \cdot 10^{33}\, a, 90\,\%\,\mathrm{CL}) \tag{4.3}$$

$$p \to \mu^+ + \pi^0 \, (\tau > 6.6 \cdot 10^{33}\, a, 90\,\%\,\mathrm{CL}) \tag{4.4}$$

It is not expected that LENA will improve these limits significantly [21]. On the other hand, most supersymmetry (SUSY) models favor the decay mode into a Kaon, where the limit comes from Superkamiokande as well [26]:

$$p \rightarrow K^+ + \bar{\nu}\,(\tau > 2.3 \cdot 10^{33}\,a, 90\,\%\,\mathrm{CL}) \tag{4.5}$$

This channel is the golden proton decay channel in a liquid scintillator detector, as the sensitivity of this channel is an order of magnitude larger than in water Cherenkov detectors. Due to delayed coincidence events of the kaon's decay products and pulse shape analysis, this channel is expected to be background-free for about ten years. This would allow to improve the limit to: $\tau > 4 \cdot 10^{34}\,a\,(90\,\%\,\mathrm{CL})$.

Chapter 5

Channel discrimination in LENA

Ideally, a neutrino detector would measure the flavor-, energy- and time-resolved neutrino event rate of a SN on an event-by-event basis. In reality, one has to deal with the uncertainties arising from event reconstruction and leading to limited knowledge on the SN properties. The key goal of SN neutrino observations is to measure time- and flavor-dependent features of the signal. The studies described in this chapter investigate the efficiencies for neutrino flavor identification of SN neutrinos in LENA. The strategy for this discrimination is based on the different available neutrino detection channels in LENA described in section 5.1. In section 5.2 the expected event rate in LENA is determined from the time-integrated neutrino signal. Subsequently, the discussion moves on to the creation of a Monte Carlo dataset for a SN neutrino signal in LENA in section 5.3. In section 5.4 a strategy on channel discrimination in LENA is presented and its efficiency is discussed. Section 5.5 focuses on the time-resolved SN event rate and the channel discrimination in this case.

5.1 Detection channels for SN neutrinos in LENA

This section discusses the SN neutrino detection channels in LENA. A liquid scintillator based detector has several detection channels for SN neutrinos. Overall, LENA provides six detection channels, three charged current (CC) channels as well as three neutral current (NC) channels. Table 5.1 gives an overview over the detection interactions, energy thresholds and possible subsequent reactions. The energy-dependent cross sections for the detection interactions in the expected energy region for SN neutrinos are plotted in figure 5.1.

No.	Type	Interaction	Subsequent Reaction	E_{trh} [MeV]
1	CC	$\bar{\nu}_e + p \rightarrow n + e^+$	$n + p \rightarrow d + \gamma$	1.8
2	CC	$\bar{\nu}_e + {}^{12}\mathrm{C} \rightarrow e^+ + {}^{12}\mathrm{B}$	${}^{12}\mathrm{B} \rightarrow {}^{12}\mathrm{C} + e^- + \bar{\nu}_e$	14.4
3	CC	$\nu_e + {}^{12}\mathrm{C} \rightarrow e^- + {}^{12}\mathrm{N}$	${}^{12}\mathrm{N} \rightarrow {}^{12}\mathrm{C} + e^- + \nu_e$	17.3
4	NC	$\nu + {}^{12}\mathrm{C} \rightarrow \nu + {}^{12}\mathrm{C}^*$	${}^{12}\mathrm{C}^* \rightarrow {}^{12}\mathrm{C} + \gamma$	15.1
5	NC	$\nu + e^- \rightarrow \nu + e^-$	-	($\sim$0.2)
6	NC	$\nu + p \rightarrow \nu + p$	-	($\sim$0.2)

Table 5.1: CC and NC detection interactions in LENA with energy thresholds and subsequent reactions. Channel 5 and 6 do not have any intrinsic energy threshold. However, due to background from the beta decay of ^{14}C an energy cut at about 0.2 MeV is necessary. Further details on the background of ^{14}C can be found in section 5.2.2.

Channel 1: Inverse Beta Decay (IBD)

This detection channel is exclusively sensitive to $\bar{\nu}_e$. It is the interaction with the highest cross section and provides the highest event rate of all channels in LENA. Another advantage of this channel for analysis is the clear coincidence signal of the delayed neutron capture. Neutrons are captured on hydrogen after an average time of 0.25 ms and create mono-energetic photons of 2.2 MeV. Average displacement of the capture vertex relative to the position is 17 mm [27]. Because of the large statistics and the clear identification the IBD is the "golden" detection channel in LENA. The energy threshold of 1.8 MeV results from the mass differences of the initial and final state particles. Another feature is the lightly anisotropic spatial distribution of the IBD positrons, which could be in principle used for pointing to the SN in a high-statistics measurement [28].

Channel 2: CC interaction of $\bar{\nu}_e$ on ^{12}C ($\bar{\nu}_e$-^{12}C)

This interaction is another exclusive detection channel for $\bar{\nu}_e$. Because of the higher energy threshold of 14.4 MeV and a lower cross section the event rates are substantially lower compared to the IBD. The subsequent beta decay of ^{12}B with a half-life of 20.2 ms and a Q value of 13.4 MeV provides a coincidence signal, that can be used to identify this channel. Since the ν_e-^{12}C has a similar coincidence signal, separation of those two signals are challenging.

Channel 3: CC interaction of ν_e on ^{12}C (ν_e-^{12}C)

This CC interaction is an exclusive detection channel for ν_e. Compared to the CC-^{12}C channel for the $\bar{\nu}_e$ it has an even higher energy threshold of 17.3 MeV. The subsequent beta decay of ^{12}N provides a coincidence signal with a half-life of 11.0 ms and a Q value of 16.3 MeV. Separation from the $\bar{\nu}_e$-^{12}C is challenging due to the similar signature.

Channel 4: NC scattering on ^{12}C (NC-^{12}C)
This NC interaction on ^{12}C is accessible to all neutrino flavors. In this interaction neutrinos excite the 15.1 MeV state of ^{12}C which subsequently leads to the emission of mono-energetic photons. Hence, this detection channel provides no spectral information. However, the mono-energetic photons can be used for the identification of this channel.

Channel 5: Elastic scattering on electrons (ν-e or ES)
The electron scattering channel is sensitive to all neutrino flavors. In general, there is no energy threshold, but due to background from the beta decay of ^{14}C, an energy cut at about 0.2 MeV is necessary. Further details on the background of ^{14}C can be found in section 5.2.2. Electrons are mainly scattered forward in this interaction, but the directional information in liquid scintillator might be hard to obtain [29].

Channel 6: Elastic scattering on protons (ν-p)
The proton scattering channel is sensitive to all neutrino flavors. The recoil energy of the scattered proton is quenched in scintillator, which means that the light output is significantly lower compared to an electron of the same energy. More details on quenching in scintillator can be found in section 4.1.1. Like the ES channel there is no intrinsic energy threshold but the background from the beta decay of ^{14}C forces a cut at a visible energy of about 0.2 MeV. Further details on the background of ^{14}C can be found in section 5.2.2. This channel is expected to have the second highest statistics in LENA [30,31]. However, the effective event rate is strongly dependent on the energy cut.

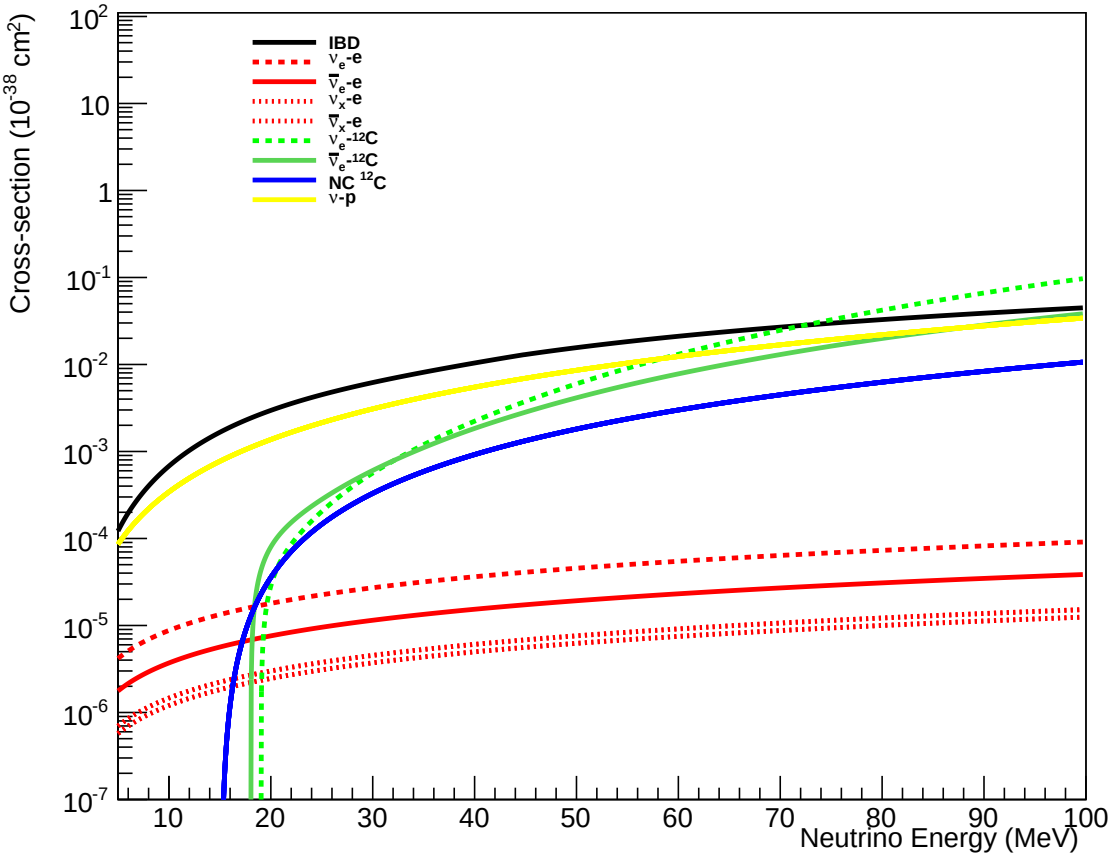

Figure 5.1: Cross sections of the important SN neutrino detection channels in LENA as a function of neutrino energy. References: IBD [32], ν-e [33], CC-^{12}C [34], NC-^{12}C [35], ν-p [31].

5.2 SN event rate in LENA

The first step in the analysis of flavor identification via the discrimination of detection channels is to calculate the number of events for each channel in the case of a SN detected by LENA. The number of events per channel depends on the neutrino flux at the Earth, the cross section of the respective interaction and the number of targets available in LENA. Multiplication of the input neutrino fluxes and cross-sections gives the interaction rates as function of neutrino energy. To consider the limited energy resolution of the detector one has to fold also with the detector response and obtains (smeared) rates as function of detected energy, i.e. the event spectrum visible in the detector. Computation of event rates has been performed with the software package SNOwGLoBES[1] [36,37]. The schematic dataflow in SNOwGLoBES is shown in figure 5.2. However, the ν-p channel is not included in this framework and had to be calculated separately. The even rate for

[1]SNOwGLoBES: SuperNova Observatories with GLoBES

the ν-p channel is presented in section 5.2.1.

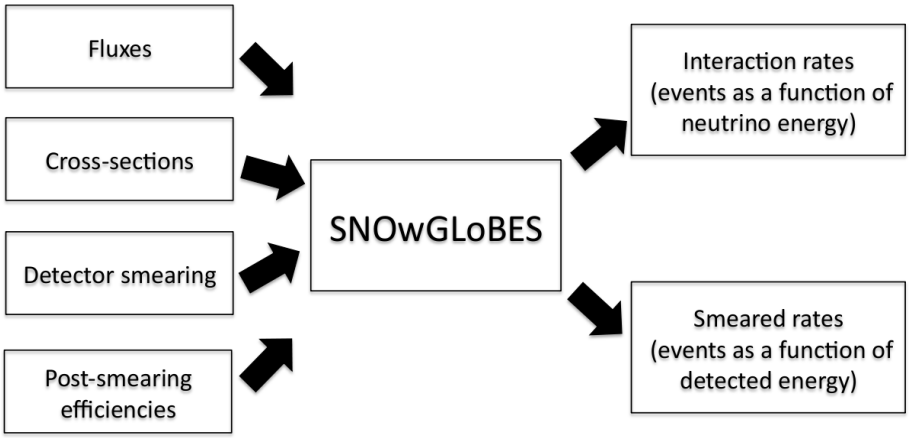

Figure 5.2: Schematic dataflow in SNOwGLoBES. By multiplying neutrino fluxes and cross-sections one calculates the interaction rates as function of neutrino energy. With the inclusion of detector smearing and post-smearing efficiencies one calculates smeared rates as function of detected energy. [36]

The model for the neutrino flux on Earth provided in SNOwGLoBES and used in this section is the GVKM[2] model [38]. To be accurate, it is not a flux but a fluence, which is the flux integrated over the time of the burst (about 10 s). The distance assumed for the SN in this calculation is 10 kpc. In figure 5.3 the GVKM fluence at Earth is plotted. The energy-dependent cross sections have already been discussed in section 5.1 and a plotted in figure 5.1. The energy resolution for liquid scintillator is determined by the statistical error of the measured number of photoelectrons N_{pe}: $\Delta E/E = N_{pe}(E)^{-1/2}$. The expected N_{pe} for LENA is at least 200 photoelectrons per MeV leading to a energy resolution of about 7 % at 1 MeV [21]. This energy resolution is also assumed in SNOwGLoBES. The number of events for 50 kt of LAB in LENA have been calculated and are shown in table 5.2. Furthermore, the event spectrum as a function of neutrino energy is shown in figure 5.4(a), and the visible energy spectrum in figure 5.4(b).

[2]GVKM: Gava-Kneller-Volpe-McLaughlin

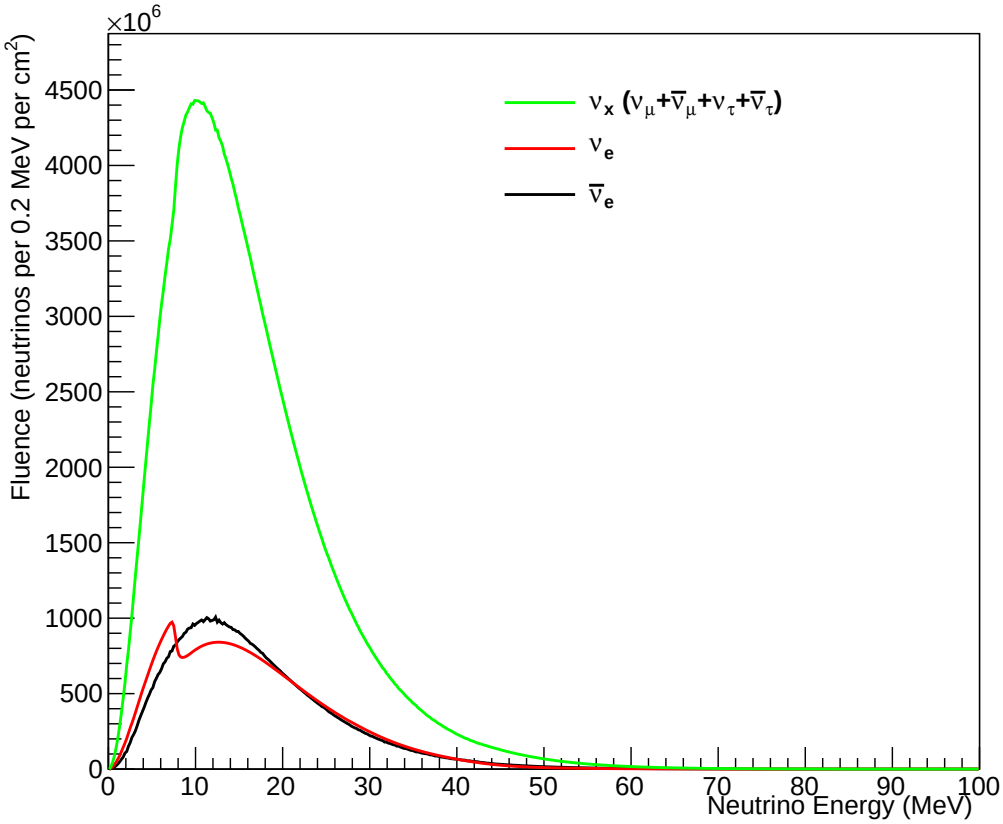

Figure 5.3: The GVKM fluence (integrated flux over time of SN burst) at Earth for the different neutrino flavors assuming a SN distance of 10 kpc. This model includes collective oscillation effects, which are visible in the ν_e curve. [38]

Channel	**Type**	**Number of events**
IBD	CC	9250
NC-^{12}C	NC	1296
ν-e	NC	496
ν_e-^{12}C	CC	468
$\bar{\nu}_e$-^{12}C	CC	459
Total number of events		11969

Table 5.2: Number of events per channel in 50 kt of LAB calculated for a SN burst at a distance of 10 kpc based on the GVKM model.

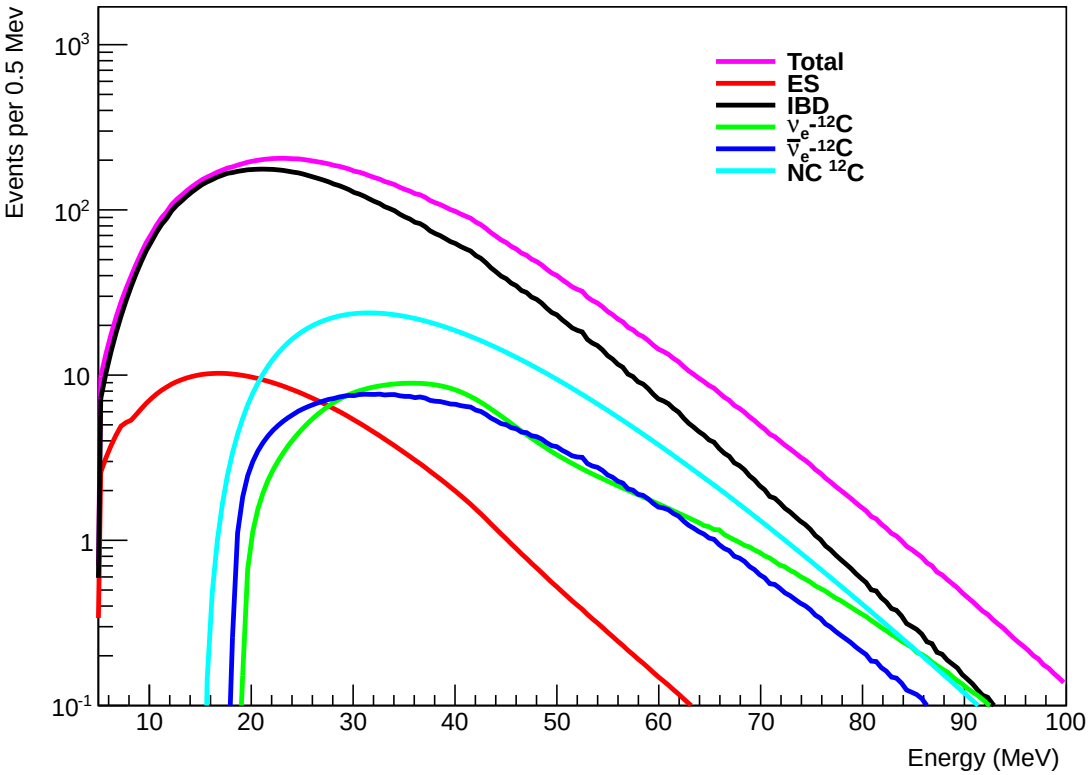

(a) Expected event spectrum for the different detection channels in 50 kt LAB as function of neutrino energy using the GVKM model.

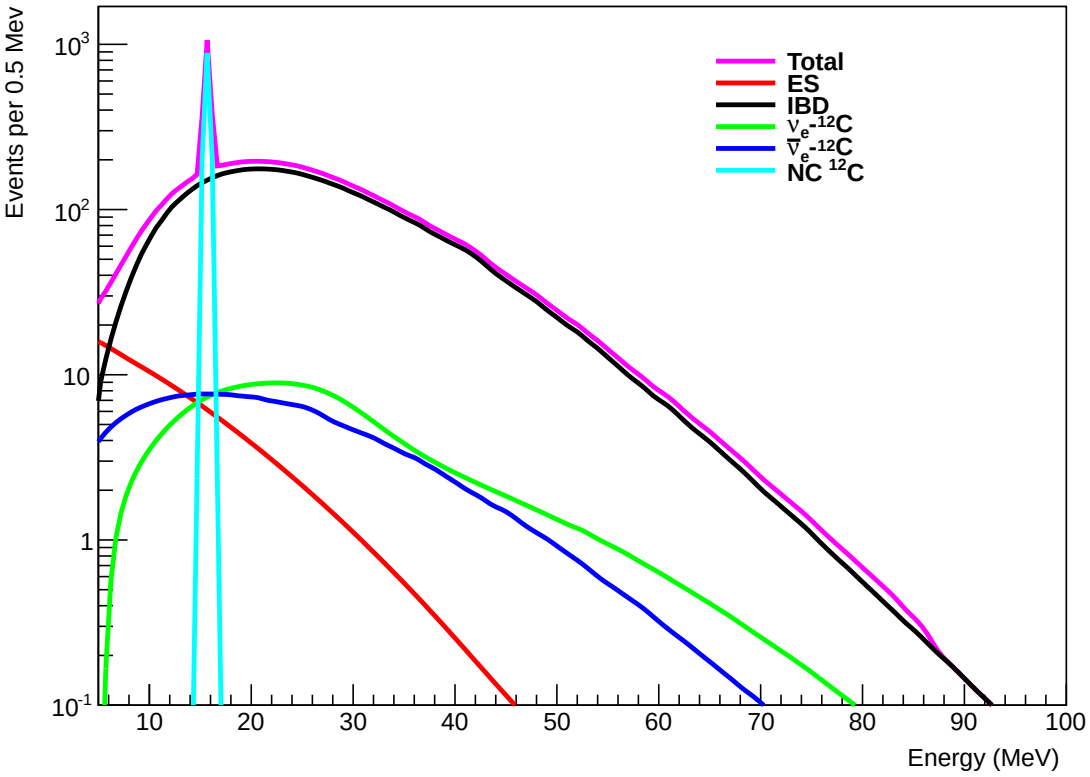

(b) Smeared event spectrum for the different detection channels in 50 kt LAB as function of visible energy using the GVKM model.

Figure 5.4: Interaction rates and smeared rates

5.2.1 Event rate of the ν-p channel

Detection of SN neutrinos via the elastic scattering on protons has been particularly investigated by J.F. Beacom et al. [30,31]. The studies on the ν-p channel in LENA base on work of Lukas Hoppenau done in his bachelor thesis [39]. This detection channel potentially provides high statistics but the rate depends crucially on the energy threshold of the detector. This threshold is expected to be about 200 keV resulting from the background of the decay of ^{14}C. The expected background from ^{14}C in LENA is studied in section 5.2.2.

Recoil protons are quenched, which means that the scintillation light output is lower compared to the output of an electron with the same energy (cf. section 4.1.1). The Birks constant in Birks law (cf. equation 4.1) is assumed to be 0.01 g/(cm^{2}MeV) in this thesis and references to measurements of Borexino [31]. In figure 5.5 the quenched energy as function of proton recoil energy is plotted.

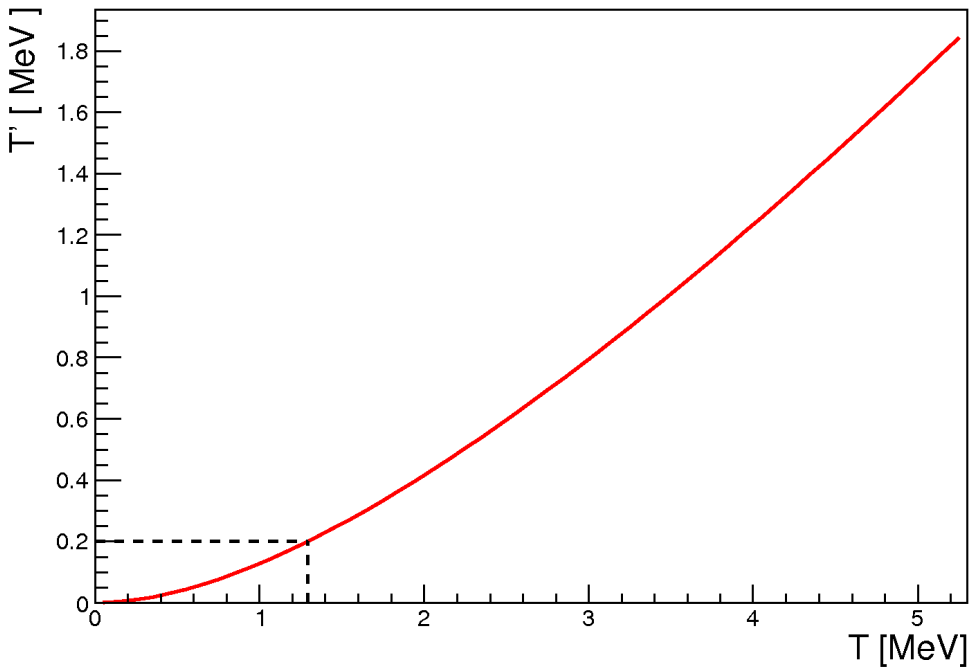

Figure 5.5: Quenched energy T$'$ as function of the proton recoil energy T based on measurements of protons in scintillator. The dashed line depicts the quenched energy of 0.2 MeV corresponding to a proton recoil energy of about 1.25 MeV. The plot has been taken from [39].

Due to this quenching, the visible energy spectrum is shifted to low energies compared to other channels. The smeared rates for the ν-p channel are plotted in figure 5.6. The calculated number of events of all detection channels including the ν-p channel are shown in table 5.3.

Channel	Type	Number of events
IBD	CC	9250
ν-p	NC	4179
NC-^{12}C	NC	1296
ν-e	NC	496
ν_e-^{12}C	CC	468
$\bar{\nu}_e$-^{12}C	CC	459
Total number of events		16148

Table 5.3: Number of events calculated for a SN burst at a distance of 10 kpc for the different detection channels including the ν-p channel in 50 kt LAB using the GVKM model.

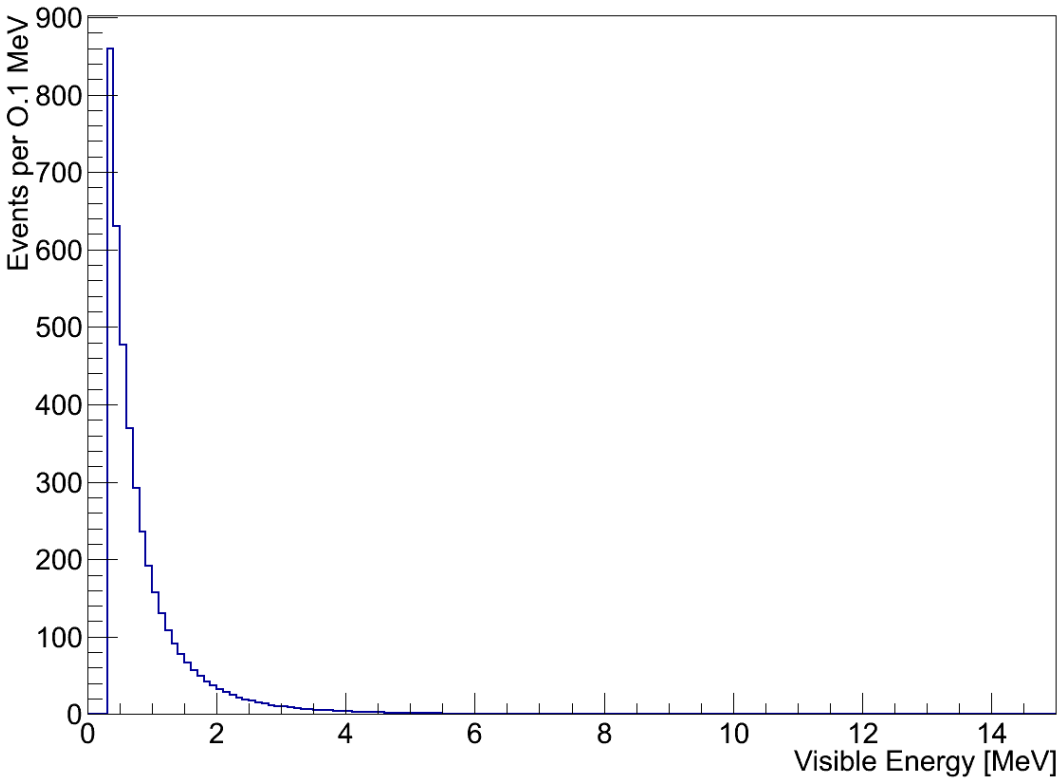

Figure 5.6: Number of events for the ν-p channel in 50 kt LAB as function of visible energy for the GVKM model. The spectrum below 0.2 MeV has been cut off, due to expected background from the decay of ^{14}C.

5.2.2 Expected background from the decay of ^{14}C

The background of the beta decay of ^{14}C determines the energy cut for the ν-p channel and the ν-e channel. This isotope is produced in the Earth's atmosphere and integrated in living organisms in a typical concentrations of one ^{14}C per 10^{12} ^{12}C. With a half-life of about 5700 years, ^{14}C is the sole unstable isotope that has to be considered for background studies out of all possible isotopes of hydrogen and carbon. Since the formation of petroleum from biomass is a long process compared to the half-life of ^{14}C, the concentration in the scintillator, which is a petroleum derivate, will be significantly lower. Borexino measured a ^{14}C/^{12}C ratio of $(1.94 \pm 0.09) \cdot 10^{-18}$ [40]. The endpoint of ^{14}C beta spectrum marks the value for the energy cut. The endpoint is at 156 keV but because of the limited energy resolution the visible endpoint of the beta decay is higher.
In the following, the number of background events of ^{14}C within the time scale of a SN burst is estimated. First, the absolute number of ^{12}C atoms is estimated. Assuming an active mass of 51 kt of LAB ($C_{18}H_{30}$) the number of ^{12}C (N_{C12}) are calculated as follows:

$$N_{C12} = n_{C12} \cdot \frac{M}{m_{LAB}} \cdot N_A = 18 \cdot \frac{(51 \cdot 10^9)\,g}{241\,\frac{g}{mol}} \cdot 6.02 \cdot 10^{23}\,mol^{-1} \approx 2.29 \cdot 10^{33} \qquad (5.1)$$

where n_{C12} denotes the number of ^{12}C atoms per LAB molecule, M the total mass of LAB in LENA, m_{LAB} the molecular mass of LAB and N_A the Avogadro constant. Multiplying the n_{C12} with the concentration of ^{14}C gives the absolute number of ^{14}C (N_{C14}). In table 5.4, N_{C14} and the number of background events for different concentrations of ^{14}C are shown. Subsequently, the visible energy spectrum from the beta decay of ^{14}C has been simulated for 10^6 events in LENA. The result is plotted in figure 5.7. To investigate the number of events near the endpoint, the reconstructed energy spectrum has been plotted logarithmically.

Ratio of ^{14}C/^{12}C	N_{C14}	Number of events in 10 s
$20 \cdot 10^{-18}$	$45.9 \cdot 10^{15}$	$17.70 \cdot 10^5$
$10 \cdot 10^{-18}$	$22.9 \cdot 10^{15}$	$8.85 \cdot 10^5$
$5 \cdot 10^{-18}$	$11.5 \cdot 10^{15}$	$4.42 \cdot 10^5$
$2 \cdot 10^{-18}$	$4.6 \cdot 10^{15}$	$1.77 \cdot 10^5$

Table 5.4: Number of background events from the beta decay of ^{14}C for different concentrations of ^{14}C in 10 s assuming 51 kt of LAB.

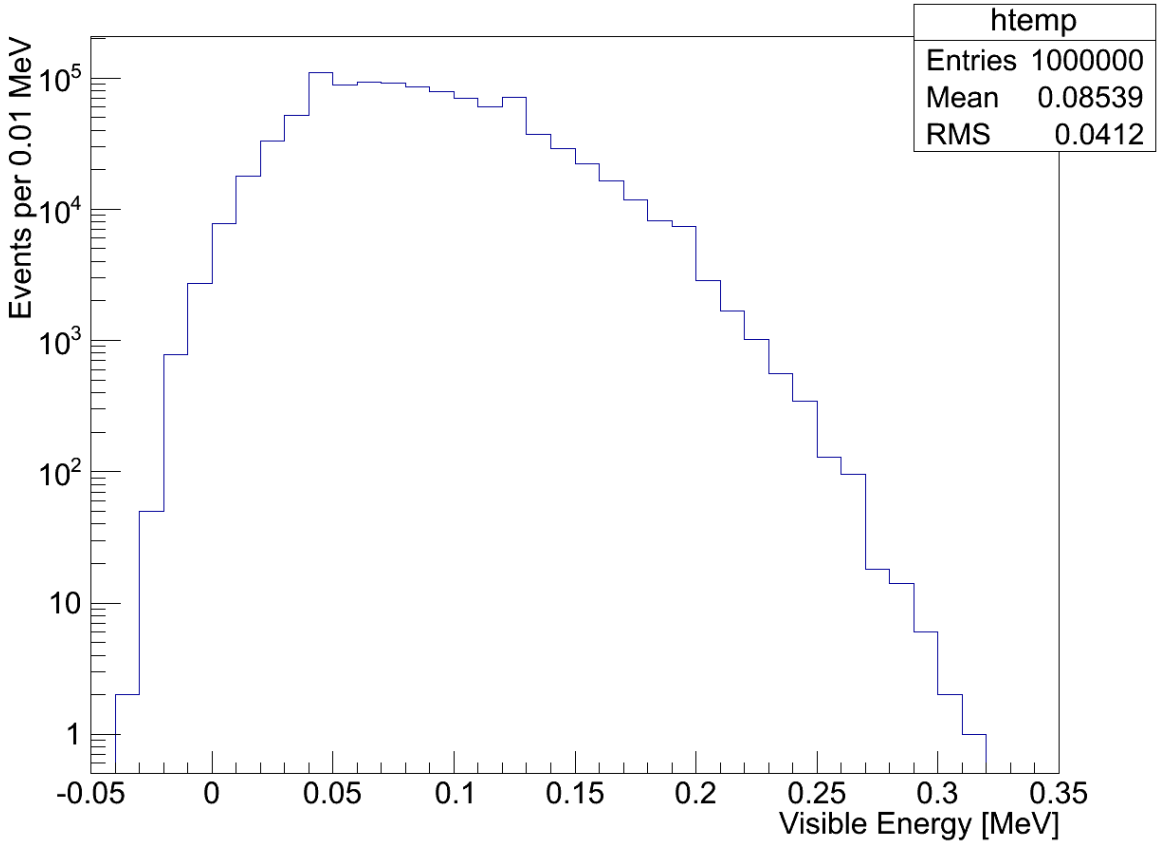

Figure 5.7: Reconstructed energy spectrum of the ^{14}C beta decay in LENA. For this plot 10^6 events have been simulated which corresponds to the number of events for a $^{14}C/^{12}C$ ratio of about $11.4 \cdot 10^{-18}$ in 51 kt LAB in 10 s. To focus on the region near the endpoint of the reconstructed energy the spectrum has been plotted logarithmically. Events with negative energies are probably due to false energy corrections within the energy reconstruction algorithm.

The number of events drops below 1000 events per 0.01 MeV at 0.23 MeV. Between 0.2 MeV and 0.3 MeV there are 6556 events which would be about 6 times the rate of the proton scattering event rate. Above 0.25 MeV there are about 266 events. Above 0.3 MeV there are basically no events. Based on this estimate it seems that the threshold of 0.2 MeV needs to be shifted to 0.25 MeV for relative low background or to 0.3 MeV for basically no background. These numbers are for a $^{14}C/^{12}C$ ratio of about $11.4 \cdot 10^{-18}$. If one could reach the $^{14}C/^{12}C$ ratio of Borexino [40] the number of events would roughly drop by a factor of 5.

5.3 Dataset for channel discrimination

The next step in the analysis of channel discrimination is to simulate a dataset reflecting the measurement of a SN in LENA. Therefore, a Monte Carlo simulation has been

programmed using the ROOT framework [41]. The following assumptions were made:

- The number of events for each detection channel has been calculated in the last section and is presented in table 5.3. These numbers have been used for the creation of a dataset.
- The distribution of visible energy for each detection channel has been simulated on the basis of SNOwGLoBES and is shown in figure 5.4(b). For the ν-p channel the energy spectrum is shown in figure 5.6.
- The position distribution is assumed to be uniform in the cylindrical detector (height: 96 m, radius: 14 m). The position resolution in x and y direction is $\sigma_{xy} = 83\,\text{mm}$ and in z direction $\sigma_z = 100\,\text{mm}$ [21]. Hence, the position has been smeared with a normal distribution using those values.
- The detection times of the events have been distributed uniformly over a time interval of 10 s. A time-dependent analysis is presented in section 5.5.
- The three CC channels feature a delayed coincidence signal which has to be included:

  In IBD, the neutron is captured on an average after 250 µs. The average displacement of the capture vertex relative to the position is 17 mm [27]. The energy resolution for the neutron capture photon of 2.2 MeV is determined by the statistical error of the measured number of photo electrons N_{pe}: $\Delta E/E = N_{pe}(E)^{-1/2}$.

  The energy spectra of the beta decays of ^{12}B and ^{12}N have been obtained with a GEANT4 [42] based simulation of the LENA detector. The time delay of the decay relative to the prompt event event has been included with a half-life of 20.20 ms for ^{12}B respectively 11.00 ms for ^{12}N.

5.4 Channel discrimination

In this section the strategy for the flavor identification via channel discrimination is described. For a SN at 10 kpc we expect about $1.6 \cdot 10^4$ events in 10 seconds. On top of that, the three CC channels produce a delayed coincidence event, which adds about 10^4 events. Hence, there are $2.6 \cdot 10^4$ events in ten seconds corresponding to a rate of 2.6 kHz or 2-3 events per ms. Before going into the details, the basic strategy is shortly presented.

1. The first step is to find the neutron capture events for tagging the IBD events.
2. Next, the beta decay events of the two CC-^{12}C channels are identified and afterwards disentangled.
3. To distinguish the NC channels energy cuts are used and pulse shape discrimination is included for optimization.

About 70 % of the SN events are associated with the IBD channel. However, the IBD channel can be effectively discriminated by tagging the fast coincidence of the neutron capture. The average delay of 250 µs is relatively short compared to the general event rate. As the photon released in the neutron capture on hydrogen takes a fixed energy of 2.2 MeV, a cut on reconstructed energy of the delayed event provides a further discrimination possibility. Finally, the reconstructed positions of neutron capture and positron from the IBD can be used for a spatial coincidence as the average neutron displacement is about 17 mm [27]. This displacement is small compared to the spatial resolution of the detector, which is thus the dominating factor for the choice of the spatial cut parameter.
The two CC-^{12}C channels feature also coincidence events via subsequent beta decays. The reconstructed position of the beta decay event can be used just like in the case of the neutron capture, as the position of the beta decay event is basically the same as for the previous CC interaction. However, the decay time constants are larger compared to the average neutron capture time, which weakens the discrimination potential. Another disadvantage is the broad energy spectrum of the delayed beta decays compared to the sharp energy peak of the neutron capture on hydrogen.
In order to optimize the selection cuts for the IBD and the CC-^{12}C channels, different combinations of cut values have been tested systematically. In this process one value has been ranged, while the other parameters have been fixed. For one combination ten different datasets have been tested. In table 5.5 the best cut values found within this study are presented.

	IBD (neutron capture)	**CC-^{12}C (beta decay)**
Spatial distance [mm]	<600/550	<500/450
Temporal difference [ms]	<3	<150
Visible energy [MeV]	1.8-2.6	<18 MeV

Table 5.5: Coincidence selection cut values for position (x,y/z direction), time and visible energy of the delayed event.

The disentanglement of ν_e and $\bar{\nu}_e$ events in the CC-^{12}C channels is challenging since the properties of their delayed beta decays are very similar. In table 5.6 the half-lifes and Q-values for ^{12}B and ^{12}N are given.

	^{12}B	^{12}N
Half-life [ms]	20.2	11.0
Q-Value [MeV]	13.4	16.4

Table 5.6: Half-lifes and Q-values of ^{12}B and ^{12}N.

In order to study how many events are associated with each channel, a simultaneous fit of the energy and the decay time spectra of the beta decays has been performed using

RooFit [43], a toolkit for ROOT [41]. In figure 5.8 the simultaneous fit of the visible decay energy (top) and the decay time (bottom) is visualized. The visible energy spectra of the beta decays from ^{12}N (blue) and ^{12}B (yellow) are fitted by a superposition of two generic decay spectra of free normalization that have been derived from Monte Carlo simulations. Simultaneously, the exponential decay functions for ^{12}N (blue) and ^{12}B (yellow) are fitted to the decay time distribution fixing the decay times and fitting the same normalization constants as for the energy spectra. The fit determines the normalization of both channels and therefore the number of ν_e and $\bar{\nu}_e$ events.

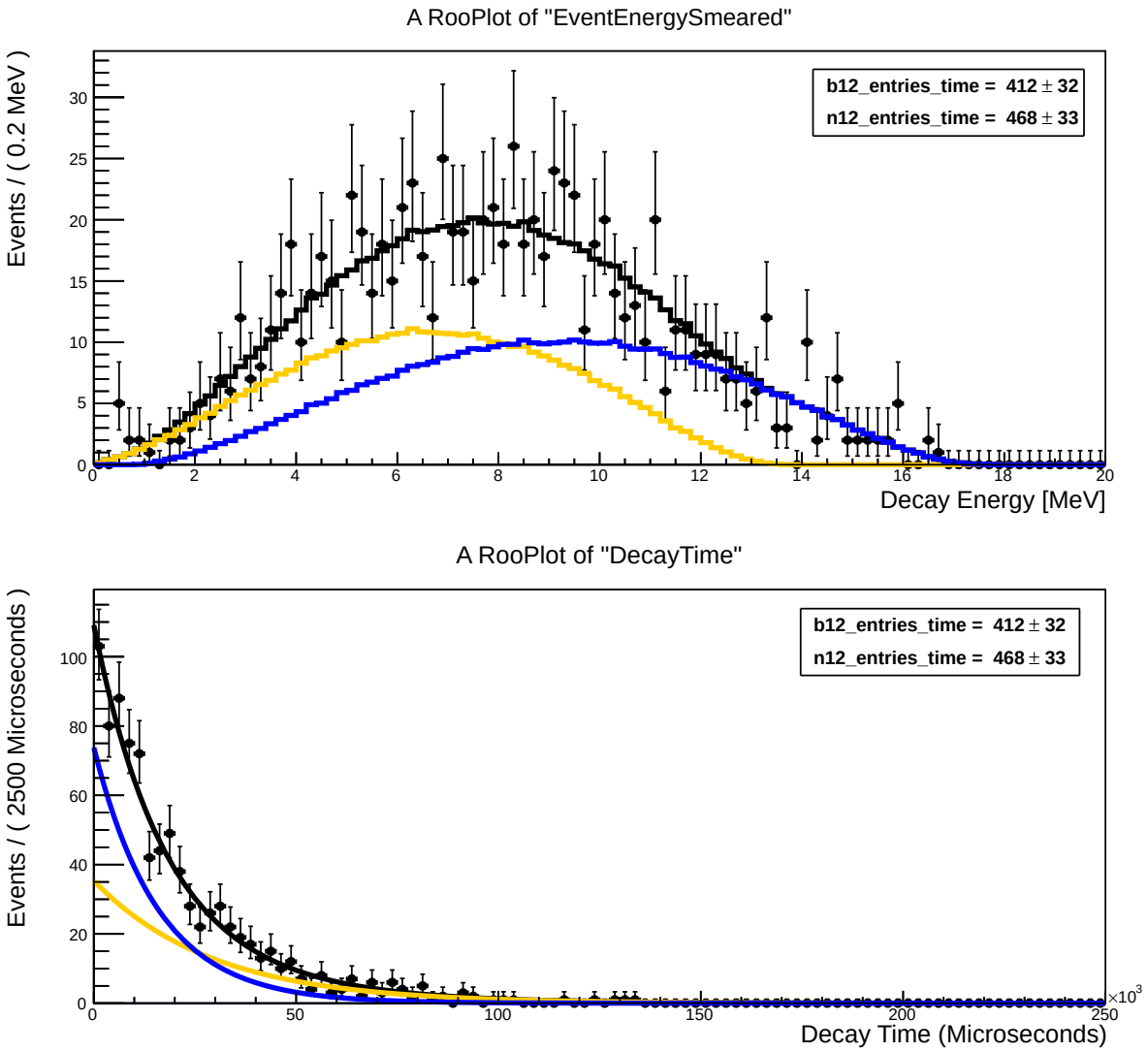

Figure 5.8: This plot visualizes the simultaneous fit of the visible decay energy (top) and the decay time (bottom) for the delayed beta decays of ^{12}N and ^{12}B in the CC-^{12}C channels. The visible energy spectra of the beta decay from ^{12}N (blue) and ^{12}B (yellow) have been simulated and are fitted to the measured overlayed energy spectrum. Simultaneously, the exponential decay functions for ^{12}N (blue) and ^{12}B (yellow) are fitted to the observed decay time distribution. The fit determines the numbers of events in each channel by the free normalization constants.

Analysis of the NC spectrum

In contrast to the CC channels, the NC channels do not provide a coincidence signature for channel discrimination. However, the NC channels feature quite different energy spectra. The combined energy spectrum of all NC detection channels is shown in figure 5.9.

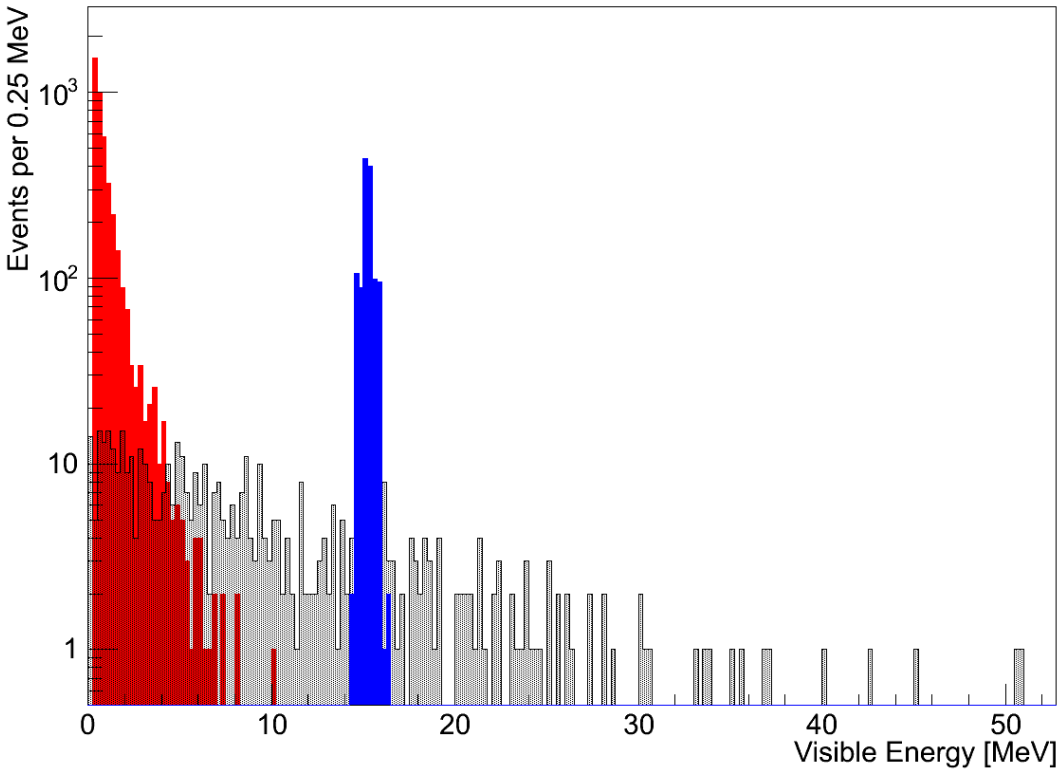

Figure 5.9: Combined event spectrum as function of visible energy for the three NC channels. The red color indicates events from the ν-p channel, the blue color denotes the events of the NC-^{12}C channel and the dark color events of the ν-e channel.

Energy cuts can be used to discriminate the NC channels. In table 5.7 the energy cuts used in this study are shown.

Channel	**Energy cut**
ν − p scattering	0 - 3.5 MeV
ν − e^- scattering	3.5 - 14.0 MeV and >16 MeV
ν − ^{12}C scattering	14.0 - 16.0 MeV

Table 5.7: Energy cut values for the three NC detection channels in LENA used for discrimination.

5.4.1 Discrimination efficiencies

In this section first results for the channel discrimination are presented. For the purpose of quantification, two quality parameters are defined as follows:

$$\text{Tagging efficiency(TE)} = \frac{\text{correctly identified events}}{\text{true number of events}} \tag{5.2}$$

$$\text{Over efficiency(OE)} = \frac{\text{falsely identified events}}{\text{correctly identified events}} \tag{5.3}$$

Once the optimal selection cut values have been found (c.f table 5.5 and table 5.7) they have been evaluated with 20 different datasets obtaining each time the tagging efficiency and over efficiency. Subsequently, the average efficiencies have been calculated and are shown in table 5.8.

Channel	**Tagging efficiency**	**Over efficiency**
IBD	>99.9%	<0.1%
CC-^{12}C	99%	1%
NC total	99%	1%
NC ^{12}C-ν	>99%	2%
NC ν-p	98%	3%
NC ν-e	$\sim$ 67%	$\sim$ 25%

Table 5.8: Average tagging efficiency (5.2) and over efficiency (5.3) for the detection channels in LENA using the number of events presented in table 5.3.

The efficiencies of the IBD are excellent. Nearly every IBD event can be tagged, while false coincidences are tagged vary rarely. This guarantees a clean measurement of the $\bar{\nu}_e$'s. Discrimination efficiencies of the CC-^{12}C channels are also fully sufficient. On average, only 1 event out of 100 cannot be tagged and 1 % of the tagged events are false. The distinction between CC-^{12}C channels has an error of about 7 %, which is surprisingly good considering the very similar coincidence signatures. The high tagging efficiency of the CC channels leads also to a very clean overall spectrum for the NC channels. Nearly all events of the NC ^{12}C-ν channel are selected based on the applied energy cut, while on average about 2 % of the event sample are falsely tagged to NC ν-e scattering events. Also the tagging efficiency for the NC ν-p channel is high as only 2 out of 100 events are not tagged. Again NC ν-e events are the most likely background: But due to the high statistics of the NC ν-p and the rather small energy range the over efficiency is low. However, the NC ν-e selection is suffering from the previous energy cuts. Only about two-thirds of the events are included with the applied energy cuts. Moreover, about every fourth event tagged is (mainly) related to the NC ν-p because of their much higher statistics. In particular this

high over efficiency of the electron scattering channel motivates the idea of pulse shape analysis presented in the next section.

5.4.2 Pulse shape analysis

Beyond the energy, timing and position criteria described before, the pulse shape of the detected events provides information useful for channel discrimination. This tool has in particular potential with regard to the discrimination between the ν-e and the ν-p channel. The photon emission process of the scintillator can be described by the superposition of several exponential decay functions (cf. 4.1.1). The exponential with the shortest time constant is often referred to as "fast component", whereas the other exponential decays are referred to as "slow components". The respective decay time constants are the same for all particles, but the weights of components can be different. In general, heavier particles, like protons or alpha particles, feature a larger light emission by the slow scintillation than electrons or photons.

Generation of event pulse shapes

To obtain the pulse shape information, protons and electrons of different energies have been generated with the GEANT4 [42] based simulation of the LENA detector. The dimensions of LENA are larger than the attenuation length of the scintillator. Therefore, the number of photoelectrons and the pulse shape measured at the PMTs depend on the position of the interaction in the detector. To remove the dependence, the number of detected photoelectrons must be rescaled based on the reconstructed position. The original pulse shape can be restored by a time-of-flight correction of the individual photons detected. In order to determine the impact of these effects, a calibration of the detector has been done before the actual analysis. For both, electrons and protons, $5 \cdot 10^4$ particles at 624 calibration points homogeneously distributed over the detector have been simulated at different energies. Afterwards the average light yield and pulse shape measured by the PMTs at each calibration point have been evaluated. The light yield and pulse shape between the calibration points is linearly extrapolated. In this simulation, LAB has been used as liquid scintillator. Furthermore, Winston cones have been simulated. Moreover, dark noise of the PMTs has been simulated with an rate of 50 per µs (which corresponds roughly to 700 Hz for a eight inch PMT). The probability of after-and late-pulses has been set to 5 %.

Up to now, the light emission of protons in LAB and the pulse shape parameters have not yet been determined precisely in laboratory experiments. Therefore, only estimated values for the relative weights of the decay time components are implemented in the simulation software. As soon as more reliable values are available, the results of this analysis are have to be reevaluated. The average pulse shape of 5000 simulated protons (red) and 5000 electrons (blue) are shown in figure 5.10(a) for 5 MeV and in figure 5.10(b) for 1 MeV.

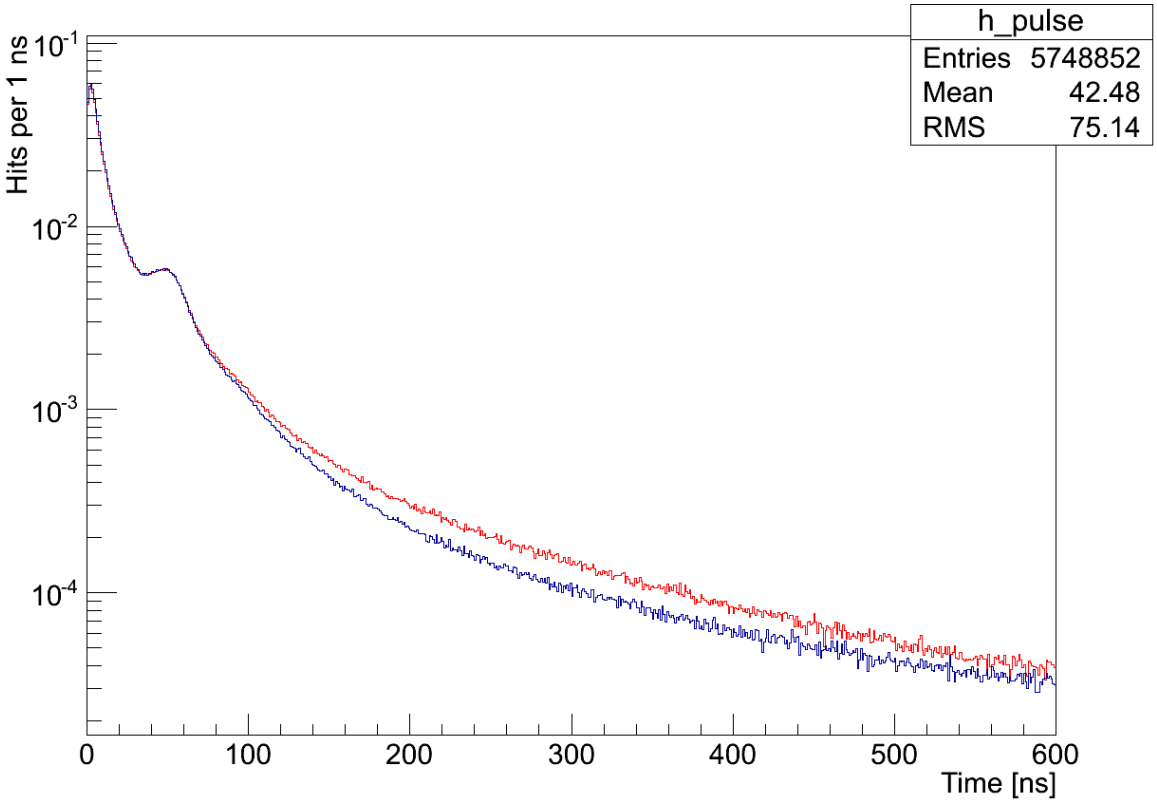

(a) Average pulse shape at 5 MeV for protons (red) and electrons (blue)

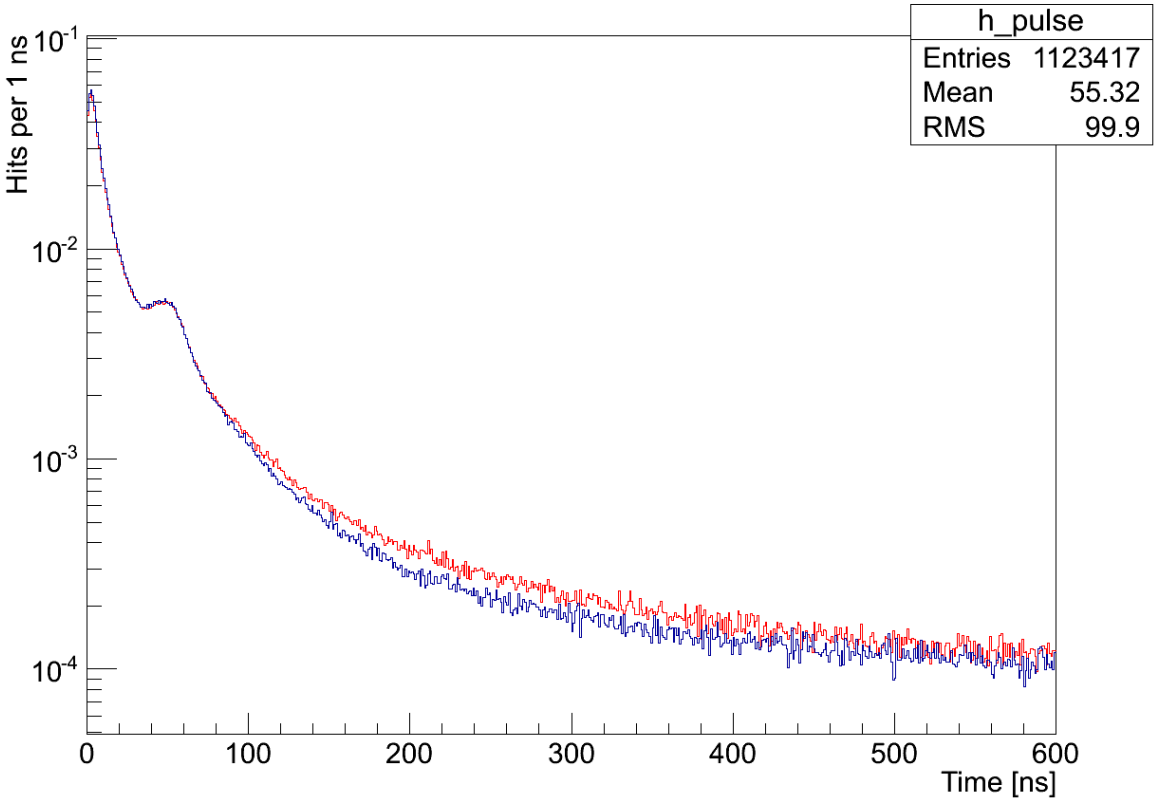

(b) Average pulse shape at 5 MeV for protons (red) and electrons (blue)

Figure 5.10: Average proton and electron pulse shapes at 5 MeV and 1 MeV

Discrimination using the tail-to-total ratio

Two main features of the average pulse shapes in figure 5.10(a) and figure 5.10(b) can be obtained. First, protons feature more hits in the tail of the pulse shape than electrons. Secondly, this characteristic is energy-dependent and more prominent at higher energies. The tail-to-total ratio (ttr), a commonly used parameter for pulse shape discrimination, is used here to evaluate the difference between the measured pulse shapes of electrons and protons. The ttr compares the relative areas of the pulse tail and the total pulse. The tail area is obtained by integration the pulse after 90 ns, while the total interval includes the whole pulse. The ttr is the ratio between these two integrals. Since protons emit more light in the slower scintillation components they feature a higher ttr. Figure 5.11 shows the ttr parameter distribution of electrons (blue) and protons (red) at six different energies from 1-6 MeV. For each energy, 10^5 protons and electrons have been simulated.

The discrimination efficiency gets better with higher energy due to more distinct pulse shapes for electrons and protons at higher energy. Table 5.9 shows the discrimination efficiencies for proton events based on a cut on the ttr parameter under the condition that the detection efficiencies for electrons is still at 95%.

Energy [MeV]	ttr efficiency [%]
1	27
2	33
3	50
4	63
5	71
6	81

Table 5.9: This table shows the percentage of proton events that can be excluded with ttr parameter under the condition that 95 % of the electron signal is included.

The main application for a pulse shape analysis is to diminish the over efficiency of the NC ν-e channel by removing NC ν-p events from the selected sample. In table 5.10 the average over efficiencies from of the NC ν-e channel in the respective energy bins are shown. Subsequently, the improvement for the over efficiency including pulse shape information are calculated, assuming a constant ttr efficiency within the energy bin. Results are shown in table 5.10 as well. Resulting from the energy cuts (c.f. table 5.7) the event energy in this channels starts at 3.5 MeV.

Energy [MeV]	Average NC ν-e OE [%]	ttr efficiency [%]	Improved OE [%]
3-4	155	50	77.5
4-5	72	63	26.6
5-6	39	71	11.3
6-7	23	81	4.4

Table 5.10: Average over efficiency and pulse shape discrimination efficiency of the NC ν-e channel in the respective energy bins. Subsequently, the improvement including the pulse shape information for the over efficiency are calculated.

To estimate the overall improvement of the over efficiency, the weight ratio of each energy bin to the total over efficiency has to be considered. Therefore, the average ratios of falsely tagged events in the respective energy bins have been investigated and are shown in 5.11. Subsequently, the weighted efficiencies have been calculated by multiplying the average ratio of over efficiency events with the ttr efficiency in the respective energy bin.

Energy [MeV]	Average ratio of OE events [%]	ttr efficiency [%]	Weighted efficiency [%]
3-4	0.33	50	16.5
4-5	0.30	63	18.9
5-6	0.17	71	12.1
above 6	0.20	81	16.2

Table 5.11: Average over efficiency and pulse shape discrimination efficiency of the ν-e channel in the respective energy bins. Subsequently, the improvement including the pulse shape information for the over efficiency are calculated.

Adding the weighted efficiencies leads to an average improvement of the discrimination efficiency of 63.7 %. Therefore the over efficiency of the NC ν-e channel is reduced from about 25 % to about 9 %.

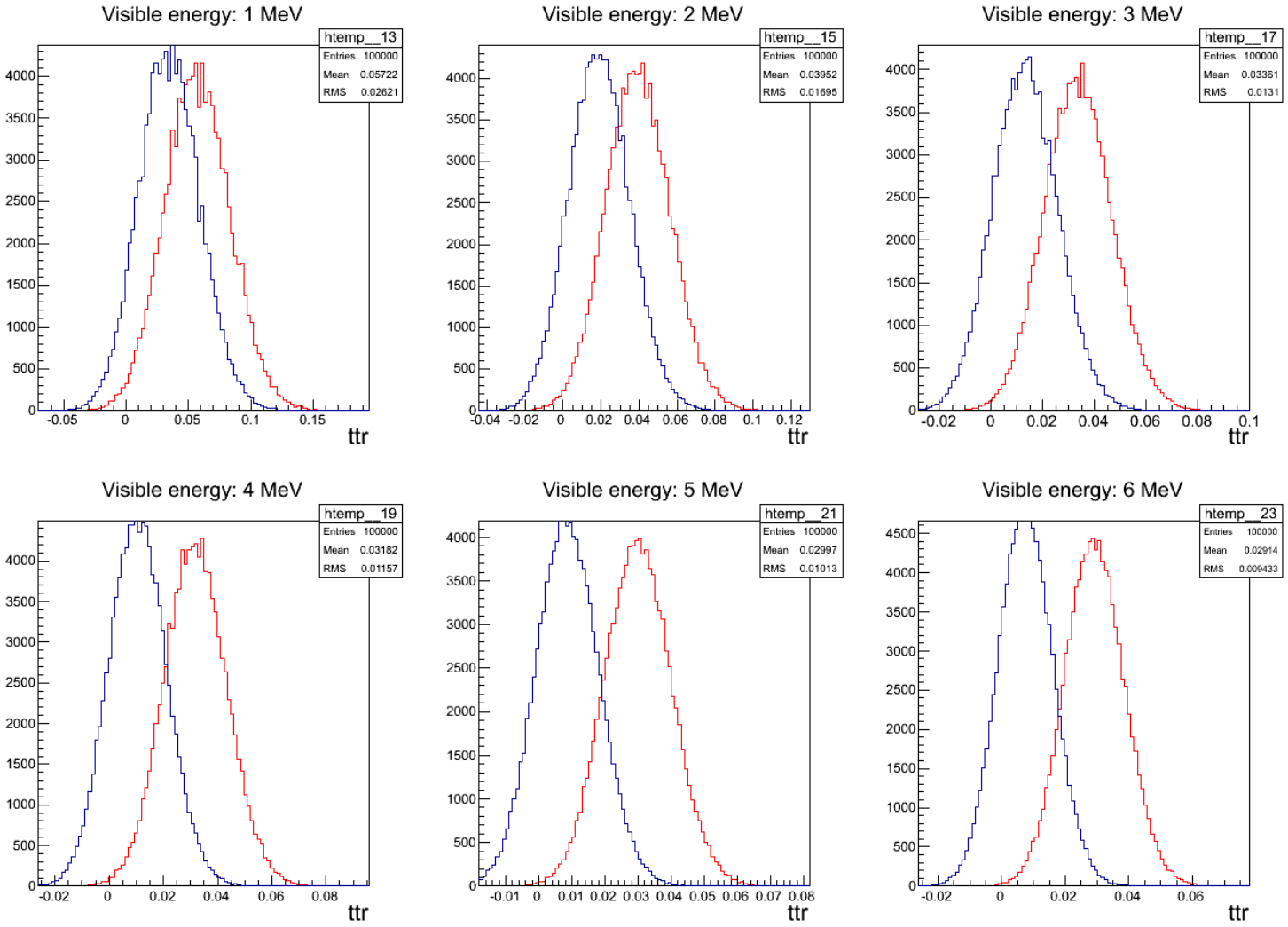

Figure 5.11: This figure shows the distribution of the ttr parameter for electrons (blue) and protons (red) at different energies. At each energy 10^5 particles have been simulated.

5.5 Time-resolved spectrum

In this section the channel discrimination introduced in section 5.4 is applied to the time-dependent neutrino signal. Since many features of SN analysis are time-dependent, the evaluation of channel discrimination for the time-dependent neutrino signal is especially important. The studies on the time-resolved event rates build on [39]. The time-resolved event rate is evaluated by describing the continuous curves for luminosities and neutrino mean energies presented in figure 3.2 by 50 discrete bins. Bins of variable widths were applied in order to describe the main features of the signal correctly. The prompt ν_e phase has been divided into twelve bins with a bin width of 0.005 s. In the accretion phase the signal has been divided into 20 bins with a bin width of 0.05 s. The cooling phase has been divided into 18 bins with a bin width of 0.5 s. The result for the binned luminosities and mean energies are shown in figure 5.12. This analysis is based on the Basel model [20] which can be seen in figure 3.2 and therefore results are not directly comparable with the results in section 5.4.

Thereupon, the neutrino fluxes at Earth have been calculated for every bin and used as input fluxes for SNOwGLoBES to calculate the number of events and the energy spectrum for the detection channels per bin. The event rates per bin are shown in table A.1 for the neutronization phase, in table A.2 for the accretion phase, and in table A.3 for the cooling phase.

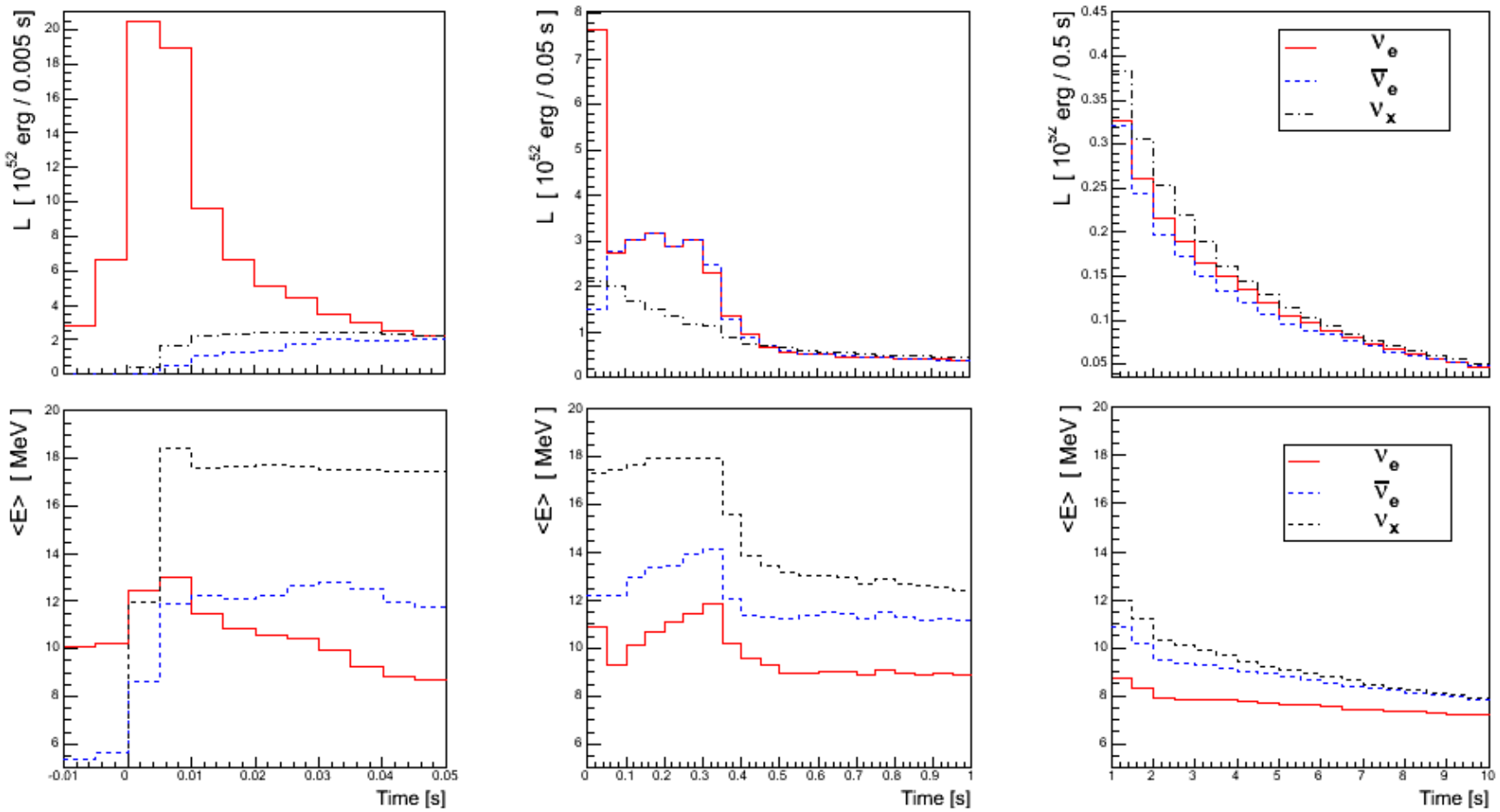

Figure 5.12: Binned luminosities and mean neutrino energies of a SN as function of time. The data bases on the Basel model shown in figure 3.2. All quantities are in the laboratory frame of a distant observer at 10 kpc from the SN. Left: Prompt ν_e. burst Middle: Accretion phase. Right: Cooling phase. This figure has been taken from [39].

The channel discrimination introduced in section 5.4 has been applied to several bins of time-resolved neutrino spectrum. A high event rate is in particular challenging, since more false coincidences are probable. Therefore, the focus have been on the bins with the high event rates. In the following, the results for the time interval from 0.125 s to 0.175 s (ΔT =0.05 s) are shown, which is the time interval with the highest event rate. In table 5.12 the event rate in this time interval for the different detection channels can be seen.

Channel	**Type**	**Number of events**
IBD	CC	369
ν-p	NC	73
NC-^{12}C	NC	28
ν-e	NC	19
$\bar{\nu}_e$-^{12}C	CC	8
ν_e-^{12}C	CC	2
Total number of events		499

Table 5.12: Number of events for the different detection channels in 50 kt LAB for the time interval of 0.125-0.175 using the basel model [20].

Based on these number of events the efficiencies for channel discrimination have been calculated using the same parameters as for the time-integrated signal (c.f. 5.2 and 5.3). Furthermore, investigations with multiples of these number of events have been done, in order to test the limits of the channel discrimination. In table 5.12 the discrimination efficiencies for the number of events and the same number of events multiplied by 10 are shown.

Channel	**Tagging efficiency**		**Over efficiency**	
	Event rate	Event rate x 10	Event rate	Event rate x 10
IBD	>99.9%	>99.9%	<0.1%	0.1%
CC-^{12}C	99.9%	96%	1%	10%
NC total	99.9%	98%	<1%	<1%
NC ν-^{12}C	99.9%	98%	$\sim$ 2%	5%
NC ν-p	98%	97%	$\sim$ 10%	10%
NC ν-e	$\sim$ 60%	$\sim$ 60%	$\sim$ 8%	$\sim$ 10%

Table 5.13: The average tagging efficiencies (5.2) and over efficiencies (5.3) for the event rate in the time interval of 0.125-0.175 s and the same event rate multiplied by ten. Because of low statistics (for instance 2 events for ν_e-^{12}C) some numbers have large variances.

In case of the normal event rate, the tagging efficiencies of the IBD and CC-^{12}C channels

are similar to the time-integrated results. The IBD provides exactly the same discrimination efficiencies, while for the CC-^{12}C channels the tagging efficiency is even better and the over efficiency is identical. However, the distinction between the two CC-^{12}C channels has an error of about 12 % for the $\bar{\nu}_e$-^{12}C channel and 25 % for the ν_e-^{12}C channel. The very different efficiencies of the two channels originate from the unequal statistics of the two channels in this time interval. Since the simultaneous fit depends on preferably high statistics, the lower statistics compared to the time-integrated case explains the larger errors. Like in the time-integrated case, the high tagging efficiency of the CC channels lead to a very clean overall spectrum for the NC channels. Furthermore, the individual tagging efficiencies of the NC channels are similar to the time-integrated case. However, the over efficiencies from the NC ν-e and the NC ν-p are different and have larger variances due to the lower statistics. The event rate multiplied by ten has been investigated to test the limits of the channel discrimination. Even at this high event rate quite decent discrimination efficiencies are achieved. The IBD channels proves, once against, the strong discrimination efficiency. The tagging efficiency is only slightly lowered for the detection channels. The most prominent effect is the larger over efficiency for the CC-^{12}C channels due to an inefficient coincidence cut for this high event rate.

Chapter 6

Exploring the neutrino mass hierarchy from a SN

In this chapter, one application of a flavor- and time-resolved SN neutrino signal is studied: The exploration of the neutrino mass hierarchy. Thus, answering the question if the neutrino mass eigenstates are ordered in the normal mass hierarchy (NH, $\Delta m^2_{\text{atm}} > 0$) or in the inverted mass hierarchy (IH, $\Delta m^2_{\text{atm}} < 0$). A common difficulty for all SN neutrino analyses is that both, the assumed core-collapse physics and the neutrino oscillations physics influence the measurable signal of the neutrino burst, which can be hard to disentangle. However, there are some model-independent features of the SN neutrino signal, which can be used in studies that are presented in this chapter. Firstly, some general approaches to explore the neutrino mass hierarchy are outlined, before in section 6.1 a promising analysis probing the neutrino mass hierarchy with SN neutrinos in LENA is presented in more detail.

The most flavor-dependent and, simultaneously, rather model-independent feature is the prompt ν_e burst that provides an approach for studies on the mass hierarchy. In the normal hierarchy and assuming a "large" value of θ_{13} ($\sin^2\theta_{13} \gtrsim 10^{-3}$), the ν_e are expected to completely oscillate into ν_x [17, 44]. Therefore, the observation of a peak in the first milliseconds of the neutrino signal would rule out the normal mass hierarchy. However, the sensitivity for LENA of ν_e is limited, since the only exclusive ν_e-^{12}C channel will have a comparable low statistics for this short time interval, and future studies will be needed to precisely evaluate the physics reach.

Another approach is the search for a characteristic signature in the $\bar{\nu}_e$ channel. Since LENA has an excellent sensitivity and excellent discrimination towards $\bar{\nu}_e$ via the IBD, this approach is very promising. In the early accretion phase, the neutrino luminosities of $\bar{\nu}_e$ and ν_x are very different, as can be seen in the top row of figure 3.2. The neutrino signal would depend on the oscillation scenario, which is derived in section 6.1 basing on [45].

Still another characteristic signature in the $\bar{\nu}_e$ channel will be visible if the SN neutrino signal is detected after propagation through Earth [46]. While propagating through the Earth the $\bar{\nu}_e$ energy spectrum is modified with energy-dependent modulations shown in the right panel of figure 3.2. The frequency of the modulation depends on the distance the neutrinos propagated through Earth. The detection of such "wiggles" requires excellent energy resolution, as is provided by a liquid scintillator-based detector like LENA.

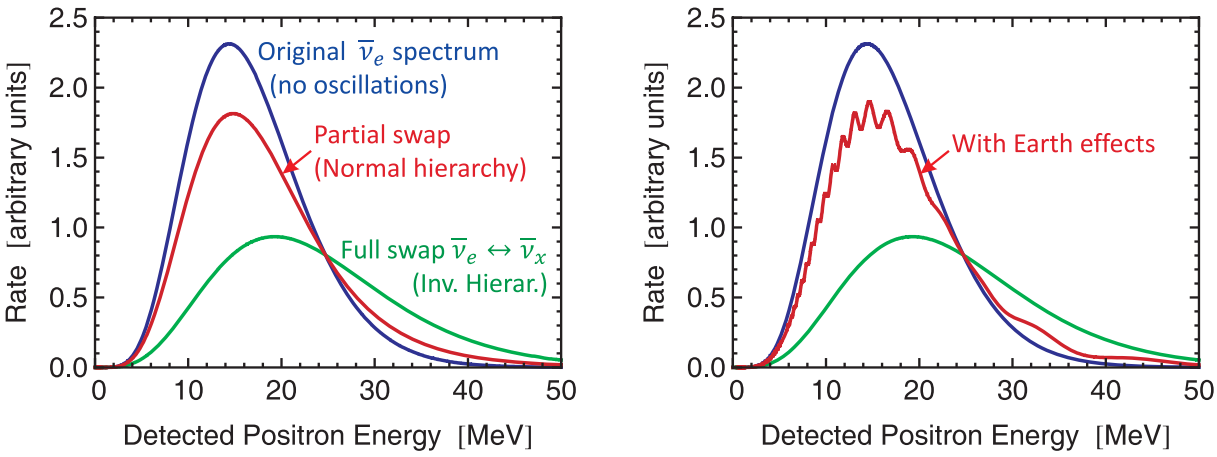

Figure 6.1: In the left panel, the $\bar{\nu}_e$ signal is shown in comparison to the oscillated signal for the normal and inverted hierarchies, as it would be observed via the IBD as function of detected positron energy. The right panel shows the energy-dependent modulations by Earth matter effects visible in the case of normal hierarchy assuming an 8000 km path through Earth. The figure is taken from [17].

6.1 Exploring the mass hierarchy with the rise time of a SN burst

In this section, an analysis on probing the neutrino mass hierarchy with the rise time of a SN burst is presented. This analysis is based on [45]. In the course of this analysis several SN models have been investigated. Most of them are provided by the Garching group [47], but also some simulations of the Basel group have been used [20]. The analysis is focused on the early evolution of the SN neutrino signal which includes the first 200 ms after the core-bounce. In figure 6.2 the neutrino luminosities L and the average neutrino energies $\langle E \rangle$ for ν_e, $\bar{\nu}_e$ and ν_x are depicted for nine 1D SN models with different progenitor masses.

There are several features that all models have in common. Before the bounce of the core (at 0.0 s) the only neutrino luminosity comes from ν_e. The production of ν_x and $\bar{\nu}_e$ sets in when the temperature is rising and the reaction in equation 3.4 for $\bar{\nu}_e$ and the reactions in equation 3.5, equation 3.6 and equation 3.7 for all neutrino flavors become efficient.

The luminosity of ν_x rises to its maximum level faster than $\bar{\nu}_e$, because the production of $\bar{\nu}_e$ is more strongly suppressed than that of ν_x during the first $\sim$20 ms after bounce. This is due to the high degeneracy of electrons and ν_e, which are present in very large numbers at this moment. The high electron degeneracy allows only for a low abundance of positrons, which suppresses the production of $\bar{\nu}_e$ by reaction in equation 3.4. Since the ν_x are only produced in NC reactions they are thermally less strongly coupled to the stellar medium and are emitted deeper inside the core (cf. section 3.1). Therefore, assuming a blackbody-like neutrino emission ($L_\nu \propto R_\nu^2 T_\nu^4$), the effective radiating surface and its luminosity of the ν_x stays on lower level compared to the electron-flavor neutrinos.

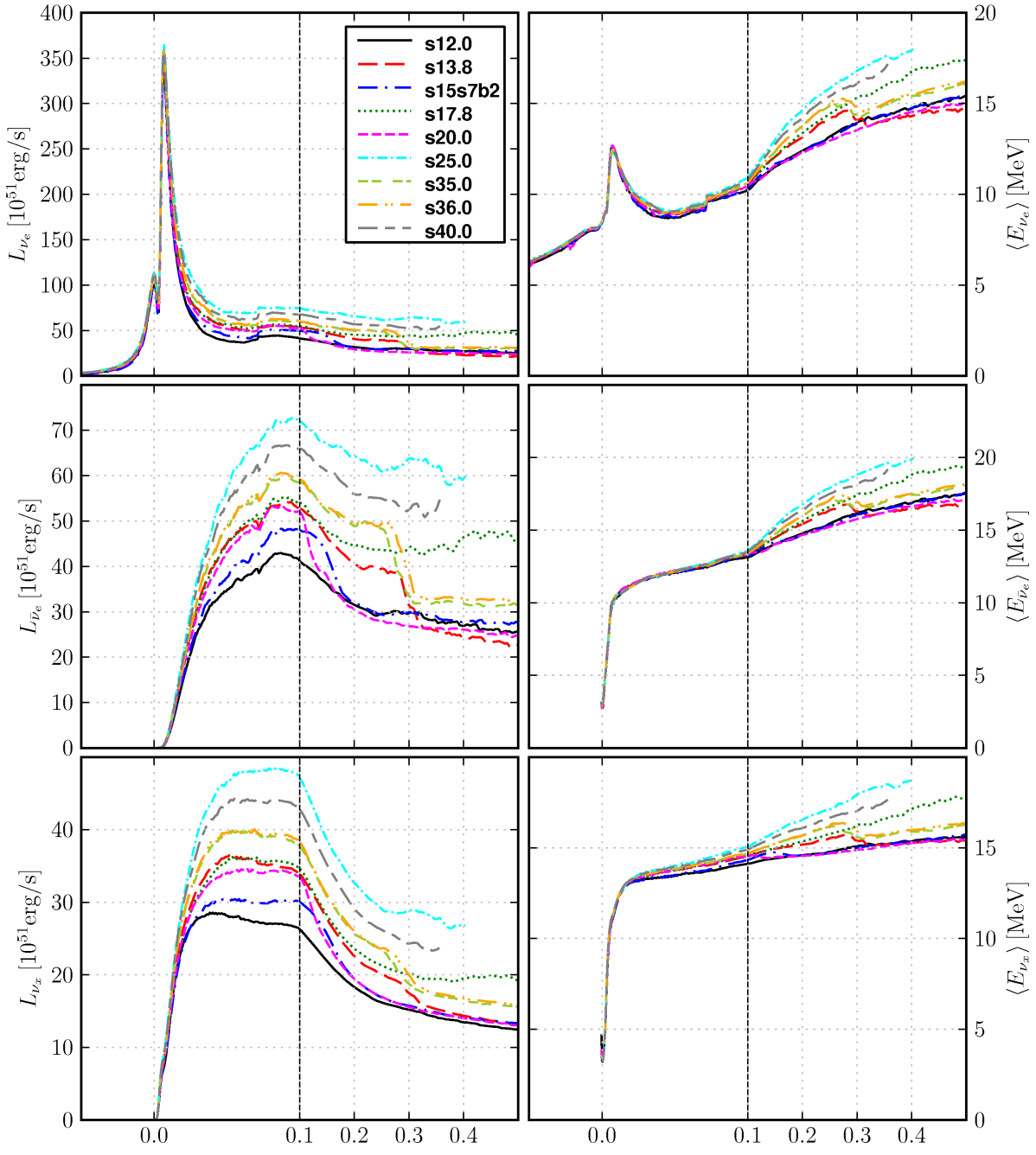

Figure 6.2: Evolution of the neutrino luminosities and the average neutrino energies for nine 1D SN models with different progenitor masses. On the x-axis the time in seconds is sketched. The vertical line marks the early timescale (100 ms). This plot is taken from [45]

.

The emitted neutrino distributions by the SN provided by the different numerical simulations are un-oscillated and doubly differential in energy and time:

$$F_\nu^0 = \frac{d^2 N_\nu}{dt\, dE} \tag{6.1}$$

where ν denotes $\{\nu_e, \bar{\nu}_e, \nu_x\}$. This is related to the time-dependent luminosity via

$$L_\nu = \int_0^\infty dE E F_\nu^0 \ . \tag{6.2}$$

The simulation output for each flavor can be factorized as follows:

$$F_\nu^0 = \frac{dN_\nu}{dt}\varphi(E_\nu) \tag{6.3}$$

where $\frac{dN_\nu}{dt}$ is the neutrino emission rate, which can be calculated from the luminosity and the mean neutrino energy $\langle E \rangle$ as follows:

$$\frac{dN_\nu}{dt} = \frac{L_\nu}{\langle E_\nu \rangle} \tag{6.4}$$

The function $\varphi(E_\nu)$ is the normalized energy spectrum. The used energy spectrum in this analysis has been taken from [48]

$$\varphi(E) = \frac{1}{\langle E_\nu \rangle} \frac{(1+\alpha)^{1+\alpha}}{\Gamma(1+\alpha)} \left(\frac{E}{\langle E_\nu \rangle} \right)^\alpha \exp\left[-(1+\alpha) \frac{E}{\langle E_\nu \rangle} \right] , \tag{6.5}$$

where the energy-shape parameter α is defined as

$$\alpha = \frac{2\langle E_\nu \rangle^2 - \langle E_\nu^2 \rangle}{\langle E_\nu^2 \rangle - \langle E_\nu \rangle^2} \, . \tag{6.6}$$

Since this analysis is focused on the different rise time of the $\bar{\nu}_e$ and ν_x signal, in figure 6.3 the luminosities, mean energies and α-fit parameters for $\bar{\nu}_e$ and ν_x of the 1D 15 $M_\odot$ model are shown.

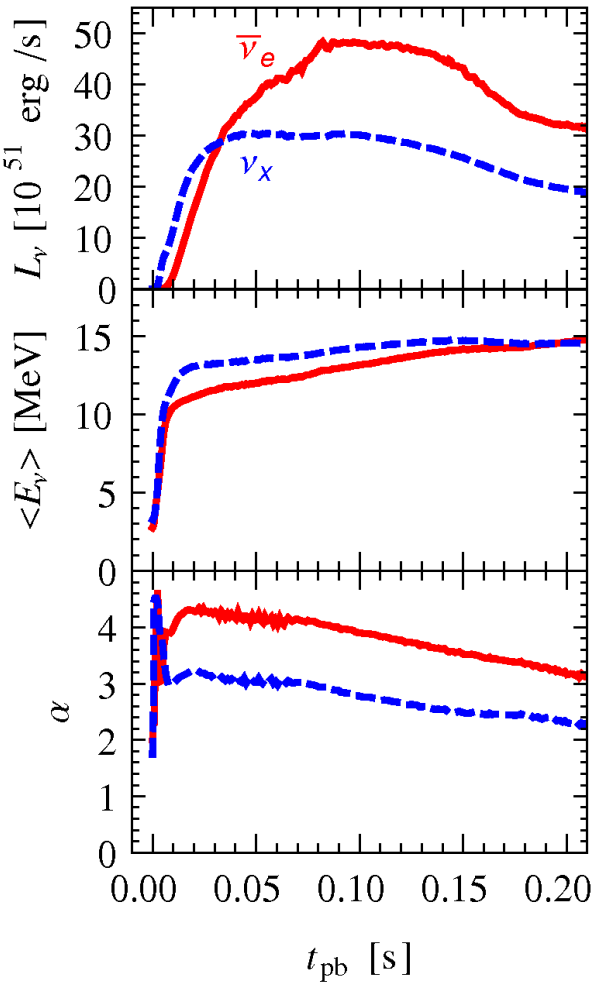

Figure 6.3: Early evolution (until 200 ms after bounce) for $\bar{\nu}_e$ (solid lines) and ν_x (dashed lines) of luminosities (top), mean energies (middle) and α-fit parameters (bottom) for the 1D 15 $M_\odot$ model.

Neutrino oscillation effects

The next step is to analyze oscillation effects on the emitted SN neutrinos. Two effects have to be taken into account for the propagating neutrinos. On the one hand the MSW oscillation effect (cf. 2.2.2) and on the other hand self-induced oscillation effects [49, 50]. Those effects take place at different radii in the star. The self-induced effects take place within $r \sim \mathcal{O}(10^3)$ km from the neutrinosphere whereas the MSW effects take place at larger radii $r \sim 10^4$–10^5 km. Since these effects are spatially separated they can be treated independently. There is a crucial difference between the NH and the IH: For the spectral ordering of the accretion phase in the NH no self-induced effects are expected whereas in IH large self-induced effects are expected [51]. However, recent studies suggest that the dense ordinary matter in the star suppresses collective oscillation in the early accretion

phase [52] [53]. Therefore, neutrinos only can undergo the MSW effects in this phase. The calculation for the $\bar{\nu}_e$ fluxes at Earth in the two different cases are derived here [54]. In the case of NH the $\bar{\nu}_e$ flux is:

$$F_{\bar{\nu}_e} = \cos^2\theta_{12} F^0_{\bar{\nu}_e} + \sin^2\theta_{12} F^0_{\bar{\nu}_x} \ , \tag{6.7}$$

while in the case of IH and assuming a "large" θ_{13} ($\sin^2\theta_{13} \gtrsim 10^{-3}$) the $\bar{\nu}_e$ flux is:

$$F_{\bar{\nu}_e} = F^0_{\bar{\nu}_x} \, . \tag{6.8}$$

Evidently, the two cases lead to a respectively different flux. In the IH, $F_{\bar{\nu}_e}$ is basically reflecting the original $F^0_{\bar{\nu}_x}$ flux, while in the NH $F_{\bar{\nu}_e}$ is more reflecting the original $F_{\bar{\nu}_e}$ flux. Since these two options show qualitative differences (in particular the already discussed different rise times) one might identify the realized neutrino mass hierarchy with the measurement of a SN signal.

Chapter 7

Conclusion and Outlook

Within this thesis, the potential neutrino signal of a SN detected by LENA has been studied. Overall, six detection channels for SN neutrinos available in LENA have been presented, along with their characteristics. Firstly, the number of events and the visible energy spectrum for the individual detection channels in LENA have been investigated assuming the GVKM SN model. It has been shown that for a SN at 10 kpc, LENA would measure about $1.6 \cdot 10^4$ events. On the basis of these calculations, datasets reflecting the measurement of a SN neutrino signal with LENA have been created by means of a Monte-Carlo simulation.

Subsequently, a strategy for event-based channel discrimination has been developed: First, the neutron capture on hydrogen is used for tagging the IBD events. Next, the beta decay events of the possible two CC-^{12}C channels are identified and afterwards disentangled by performing a simultaneous fit of the visible energy and the decay time spectra. Finally, the identification of the NC channels is reached through different cuts on the visible energy.

The IBD channel stands out with an almost perfect discrimination efficiency, as nearly every event can be tagged, while false coincidences are tagged very rarely. The tagging efficiencies for the detection channels are $\geq 98\,\%$ with the exception of the NC ν-e channel at 67 % tagging efficiency. This comparatively small tagging efficiency is due to the applied cuts on the visible energy. The over efficiencies for the detection channels are $\leq 3\,\%$, except for the NC ν-e at about 25 %. This very large over efficiency is caused by the much higher statistics of the ν-p channel.

Furthermore, the potential of pulse shape analysis, in particular with the goal to diminish the over efficiency of the NC ν-e channel, has been studied. For this purpose, the energy-dependent efficiency to discriminate between ν-e and ν-p events in the energy range from 1 MeV to 6 MeV has been investigated by using a GEANT4-based simulation of the detector. At 1 MeV only 27 % of protons can be correctly identified by the analysis of the pulse shape under the condition that the detection efficiency for the ν-e events is

at 95 %, while at 6 MeV 81 % of the protons can be discriminated. Including the pulse shape information, the over efficiency of the NC ν-e channel can be reduced from about 25 % (see above) to about 9 %.

A time-dependent SN neutrino signal, basing on the Garching model, has been created by describing the continuous neutrino luminosities and neutrino mean energies with 50 discrete bins. Subsequently, the channel discrimination has been applied to the time-dependent neutrino signal and discrimination efficiencies have been calculated and compared to the time-integrated case. The discrimination efficiencies for the CC detection channels via their coincidence events are similar to the time-integrated efficiencies. However, due to lower statistics per bin, the entanglement of the two CC-^{12}C channel suffers and the efficiencies decrease. The discrimination of the NC channels is comparable to the time-integrated signal, although the lower statistics implies greater variances.

Moreover, the background from the beta decay of the intrinsic ^{14}C has been investigated, as this background forces a cut on the visible energy. The visible energy spectrum of the beta decay have been simulated with the GEANT4-based LENA simulation. The results suggest that the energy cut has to be above 0.25 MeV for a for a sufficiently low background assuming a $^{14}\mathrm{C}/^{12}\mathrm{C}$ ratio of about $11.4 \cdot 10^{-18}$.

In addition to the above-mentioned studies on event-based channel discrimination, a possible exploration of the neutrino mass hierarchy using the SN neutrino signal has been examined. The focus has been on approaches that are relatively SN model-independent. One promising analysis is the determination of the neutrino mass hierarchy with the rise time in the early accretion phase of the SN signal. This analysis is suited for LENA with its good sensitivity and discrimination power towards the $\bar{\nu}_e$.

This thesis provides two main reference points for future studies: Firstly, studies using pulse shape analysis offer additional potential. The results of the pulse shape analysis have been successfully applied to diminish the over efficiency of the NC ν-e channel. Also, it might be valuable to reevaluate the energy cut on protons with the inclusion of the pulse shape information. Moreover, other parameters, including more sophisticated information of the pulse shape, or a multivariate approach might reach even better performances.
Secondly, the analysis of the SN neutrino signal regarding the neutrino mass hierarchy presented in this thesis offers an interesting starting point for future studies. It would be valuable to simulate the neutrino signals for the different SN models in LENA or apply different oscillation scenarios. The exploration potential for the neutrino mass hierarchy in a best case and a worst case scenario could be calculated.

Appendix A

Table of event rates for the detection channels

Bin [s]	IBD	ν-p	ν-e	ν_e-^{12}C	$\bar{\nu}_e$-^{12}C	NC-^{12}C	Sum of bin
-0.0075	0.0	0.1	1.1	0.1	0.0	0.1	1.4
-0.0025	0.0	0.2	2.5	0.4	0.0	0.3	3.4
0.0025	0.2	3.0	8.0	3.3	0.0	2.1	16.6
0.0075	5.7	11.9	7.9	3.7	0.1	5.1	34.4
0.0125	11.5	9.7	4.4	1.0	0.2	4.0	30.8
0.0175	13.3	10.0	3.3	0.5	0.2	3.7	31.0
0.0225	15.0	10.3	2.7	0.3	0.3	3.9	32.5
0.0275	19.5	10.2	2.5	0.3	0.4	4.0	36.9
0.0325	22.3	10.0	2.2	0.2	0.4	3.5	38.6
0.0375	21.3	9.6	1.9	0.1	0.4	3.5	36.8
0.0425	20.4	9.0	1.8	0.1	0.3	3.4	35.0
0.0475	20.6	8.7	1.6	0.0	0.3	3.0	34.2

Table A.1: Binned event rates in the prompt ν_e phase using the Basel model [20].

Bin [s]	IBD	ν-p	ν-e	ν_e-^{12}C	$\bar{\nu}_e$-^{12}C	NC-^{12}C	Sum of bin
0.025	156.8	83.5	36.7	6.0	2.6	33.7	319.3
0.075	292.3	80.9	19.5	0.8	4.9	30.5	428.9
0.125	339.9	75.2	20.5	1.5	6.9	28.8	472.8
0.175	368.5	73.2	19.0	2.2	8.2	27.9	499.0
0.225	334.8	66.4	17.5	2.5	7.6	25.4	454.2
0.275	366.1	62.8	19.6	3.1	9.2	24.5	485.3
0.325	305.1	58.9	15.8	2.9	8.0	22.4	413.1
0.375	136.0	21.5	9.4	0.7	2.2	10.2	180.0
0.425	87.9	8.9	6.7	0.3	1.1	5.3	110.2
0.475	68.6	6.9	5.3	0.2	0.9	4.7	86.6
0.525	56.7	5.5	4.5	0.1	0.7	3.7	71.2
0.575	52.4	4.9	4.2	0.1	0.7	3.3	65.6
0.625	50.5	4.7	4.0	0.1	0.7	3.3	63.3
0.675	46.2	4.1	3.7	0.1	0.6	2.8	57.5
0.725	43.5	3.5	3.5	0.1	0.6	2.8	54.0
0.775	43.4	3.7	3.4	0.1	0.6	2.8	54.0
0.825	40.4	3.3	3.3	0.1	0.5	2.4	50.0
0.875	38.4	3.0	3.2	0.1	0.5	2.4	47.6
0.925	37.0	2.9	3.1	0.1	0.5	2.3	45.9
0.975	35.1	2.5	2.9	0.1	0.4	1.9	42.9

Table A.2: Binned event rates in the accretion phase using the Basel model [20].

Bin [s]	IBD	ν-p	ν-e	ν_e-^{12}C	$\bar{\nu}_e$-^{12}C	NC-^{12}C	Sum of bin
1.25	298.8	17.3	26.0	0.6	3.3	15.6	361.6
1.75	212.1	8.3	20.3	0.4	1.8	9.3	252.2
2.25	156.6	3.3	16.4	0.2	1.0	5.1	182.6
2.75	134.9	2.3	14.2	0.2	0.8	3.8	156.2
3.25	116.3	1.7	12.4	0.2	0.7	3.3	134.6
3.75	101.8	1.2	10.9	0.1	0.6	2.4	117.0
4.25	90.1	0.8	9.7	0.1	0.5	1.9	103.1
4.75	79.3	0.6	8.7	0.1	0.4	1.5	90.6
5.25	70.0	0.5	7.6	0.1	0.3	1.1	79.6
5.75	63.2	0.3	6.9	0.1	0.3	1.0	71.8
6.25	58.0	0.2	6.3	0.1	0.2	1.0	65.8
6.75	53.0	0.2	5.7	0.0	0.2	0.5	59.6
7.25	48.2	0.1	5.2	0.0	0.2	0.5	54.2
7.75	42.6	0.1	4.7	0.0	0.1	0.5	48.0
8.25	39.4	0.1	4.3	0.0	0.1	0.5	44.4
8.75	36.0	0.1	4.0	0.0	0.1	0.5	40.7
9.25	33.1	0.0	3.6	0.0	0.1	0.4	37.2
9.75	30.5	0.0	3.3	0.0	0.1	0.0	33.9

Table A.3: Binned event rates in the cooling phase using the Basel model [20].

List of Abbreviations

AP	AfterPulses
BH	Black hole
Bis-MSB	Bismethylstyrylbenzene
Borexino	derived from BORon EXperiment
CC	Charged Current
CL	Confidence Level
CNO	Carbon-Nitrogen-Oxygen fusion cycle
CUPP	Center for Underground Physics in Pyhäsalmi
DAEδALUS	Decay At-rest Experiment for δ_{CP} studies At the Laboratory for Underground Sciences
DAQ	Data AcQuisition
DC	Dark Count
DM	Dark Matter
DSNB	Diffuse Supernova Neutrino Background
EC	Electron Capture
FADC	Fast Analog-to-Digital Converter
GEANT4	GEometry ANd Tracking MC platform
GLACIER	Giant Liquid Argon Charge Imaging ExpeRriment
GLoBES	General LOng-Baseline Experiment Simulator
GNO	Gallium Neutrino Observatory
GUT	Grand Unified Theories
HQE	High Quantum Efficiency
IBD	Inverse beta decay
K2K	KEK-to-Kamiokande neutrino beam
Kamiokande	KAMIOKA Nucleon Decay Experiment
KamLAND	KAMioka Liquid-scintillator Anti-Neutrino Detector
LAB	Linear Alkylbenzene
LAGUNA	Large Apparatus for Grand Unification and Neutrino Astrophyics
LENA	Low Energy Neutrino Astronomy
LINAC	LINear ACcelerator
LMA	Large Mixing Angle oscillation scenario
MC	Monte Carlo simulation
MEMPHYS	MEgaton Mass PHYSics
MSW	Mikheyev-Smirnov-Wolfenstein

NC	Neutral Current
NS	Neutron star
OC	Optical Coverage
PDE	Photo Detection Efficiency
pe	PhotoElectron
pep	Proton-Electron-Proton fusion
PMP	Phenyl-Mesityl-Pyrazoline, a fluor
PMT	PhotoMultiplier Tube
PNS	Proto-neutron star
pot	Protons On Target
pp	Proton-Proton fusion
PPO	diPhenyl-Oxazole, a fluor
PSS	PMT support structure
PXE	Phenyl-Xylyl-Ethane, organic solvent
QE	Quantum Efficiency
RPC	Resistive Plate Chamber
SiPM	SIlicon Photo Multiplier
SM	Standard Model of particle physics
SN	Core-collapse supernova
SNO	Sudbury Neutrino Observatory
SNP	Solar Neutrino Problem
SPS	Super Proton Synchrotron
SSM	Standard Solar Model
SUSY	SUper SYmmetry
T2K	Tokai-to-Kamiokande neutrino beam
TDC	Time-to-Digital Converter
TOF	Time Of Flight
ttr	Tail-to-total

List of Figures

Bibliography

[1] Y. Fukuda et al. The Super-Kamiokande detector. *Nucl.Instrum.Meth.*, A501:418–462, 2003.

[2] G. Alimonti et al. The Borexino detector at the Laboratori Nazionali del Gran Sasso. *Nucl.Instrum.Meth.*, A600:568–593, 2009.

[3] P. Alivisatos, S. Berridge, N. Bokor, C. Britton, W. Bryan, et al. KamLAND: A Liquid scintillator anti-neutrino detector at the Kamioka site. 1998.

[4] C. Amsler et al. (Particle Data Group). The Review of Particle Physics and 2009 partial update for the 2010 edition. *Phys.Lett. B*, 667:1, 2008.

[5] David J. Griffiths. INTRODUCTION TO ELEMENTARY PARTICLES. 1987.

[6] J. Schechter and J.W.F. Valle. Neutrinoless Double beta Decay in SU(2) x U(1) Theories. *Phys.Rev.*, D25:2951, 1982.

[7] Jr. Davis, Raymond, Don S. Harmer, and Kenneth C. Hoffman. Search for neutrinos from the sun. *Phys.Rev.Lett.*, 20:1205–1209, 1968.

[8] Q.R. Ahmad et al. Measurement of the rate of nu/e + d $\rightarrow$ p + p + e- interactions produced by B-8 solar neutrinos at the Sudbury Neutrino Observatory. *Phys.Rev.Lett.*, 87:071301, 2001.

[9] Samoil Bilenky. Introduction to the physics of massive and mixed neutrinos. *Lect.Notes Phys.*, 817:1–255, 2010.

[10] Boris Kayser. Neutrino mass, mixing, and flavor change. *Springer Tracts Mod.Phys.*, 190:1–24, 2003.

[11] Kei Kotake, Katsuhiko Sato, and Keitaro Takahashi. Explosion mechanism, neutrino burst, and gravitational wave in core-collapse supernovae. *Rept.Prog.Phys.*, 69:971–1144, 2006.

[12] N. Schmitz. *Neutrinophysik*. Teubner Studienbücher, 1997.

[13] D.V. Forero, M. Tortola, and J.W.F. Valle. Global status of neutrino oscillation parameters after Neutrino-2012. 2012.

[14] L. Wolfenstein. Neutrino Oscillations in Matter. *Phys.Rev.*, D17:2369–2374, 1978.

[15] S.P. Mikheev and A. Yu. Smirnov. Resonance Amplification of Oscillations in Matter and Spectroscopy of Solar Neutrinos. *Sov.J.Nucl.Phys.*, 42:913–917, 1985.

[16] Jens C. Niemeyer, M. Reinecke, and W. Hillebrandt. Models of Type Ia supernova explosions. 2002.

[17] Georg Raffelt. Neutrinos and the stars. 2012.

[18] Hans-Thomas Janka, K. Langanke, A. Marek, G. Martinez-Pinedo, and B. Mueller. Theory of Core-Collapse Supernovae. *Phys.Rept.*, 442:38–74, 2007.

[19] G.G. Raffelt. Stars as laboratories for fundamental physics: The astrophysics of neutrinos, axions, and other weakly interacting particles. 1996.

[20] T. Fischer, S.C. Whitehouse, A. Mezzacappa, F.-K. Thielemann, and M. Liebendorfer. Protoneutron star evolution and the neutrino driven wind in general relativistic neutrino radiation hydrodynamics simulations. *Astron.Astrophys.*, 517:A80, 2010.

[21] Michael Wurm et al. The next-generation liquid-scintillator neutrino observatory LENA. *Astropart.Phys.*, 35:685–732, 2012. Whitepaper for the LENA low-energy neutrino detector, 67 pages, 32 figures.

[22] H. A. Bethe. Ann. Physik 5 (1930) 325.

[23] John N. Bahcall, Aldo M. Serenelli, and Sarbani Basu. New solar opacities, abundances, helioseismology, and neutrino fluxes. *Astrophys.J.*, 621:L85–L88, 2005.

[24] J.N. Bahcall, William A. Fowler, Jr. Iben, I., and R.L. Sears. Solar neutrino flux. *Astrophys.J.*, 137:344–346, 1963.

[25] H. Nishino et al. Search for Proton Decay via p $\rightarrow$ e+ pi0 and p $\rightarrow$ mu+ pi0 in a Large Water Cherenkov Detector. *Phys.Rev.Lett.*, 102:141801, 2009.

[26] K. Kobayashi et al. Search for nucleon decay via modes favored by supersymmetric grand unification models in Super-Kamiokande-I. *Phys.Rev.*, D72:052007, 2005.

[27] M. Apollonio et al. Determination of neutrino incoming direction in the CHOOZ experiment and supernova explosion location by scintillator detectors. *Phys.Rev.*, D61:012001, 2000.

[28] P. Vogel and John F. Beacom. Angular distribution of neutron inverse beta decay, anti-neutrino(e) + p $\rightarrow$ e+ + n. *Phys.Rev.*, D60:053003, 1999.

[29] Kate Scholberg. Supernova Neutrino Detection. *J.Phys.Conf.Ser.*, 375:042036, 2012.

[30] John F. Beacom, Will M. Farr, and Petr Vogel. Detection of supernova neutrinos by neutrino proton elastic scattering. *Phys.Rev.*, D66:033001, 2002.

[31] Basudeb Dasgupta and John.F. Beacom. Reconstruction of supernova ν_μ, ν_τ, anti-ν_μ, and anti-ν_τ neutrino spectra at scintillator detectors. *Phys.Rev.*, D83:113006, 2011.

[32] Alessandro Strumia and Francesco Vissani. Precise quasielastic neutrino/nucleon cross-section. *Phys.Lett.*, B564:42–54, 2003.

[33] William J. Marciano and Zohreh Parsa. Neutrino electron scattering theory. *J.Phys.*, G29:2629–2645, 2003.

[34] E. Kolbe, K. Langanke, and P. Vogel. Estimates of weak and electromagnetic nuclear decay signatures for neutrino reactions in Super-Kamiokande. *Phys.Rev.*, D66:013007, 2002.

[35] E. Kolbe, K. Langanke, and P. Vogel. Weak reactions on C-12 within the continuum random phase approximation with partial occupancies. *Nucl.Phys.*, A652:91–100, 1999.

[36] Kate Scholberg et al. SNOwGLoBES: SuperNova Observatories with GLoBES: DRAFT. 2011.

[37] http://www.phy.duke.edu/ schol/snowglobes/.

[38] Jerome Gava, James Kneller, Cristina Volpe, and G.C. McLaughlin. A Dynamical collective calculation of supernova neutrino signals. *Phys.Rev.Lett.*, 103:071101, 2009.

[39] L. Hoppenau. Zeitaufgelöste analyse des supernova-neutrino-signals in lena. Bachelor thesis.

[40] G. Alimonti et al. Measurement of the C-14 abundance in a low-background liquid scintillator. *Phys.Lett.*, B422:349–358, 1998.

[41] R. Brun and F. Rademakers. ROOT: An object oriented data analysis framework. *Nucl.Instrum.Meth.*, A389:81–86, 1997.

[42] S. Agostinelli et al. GEANT4: A Simulation toolkit. *Nucl.Instrum.Meth.*, A506:250–303, 2003.

[43] Wouter Verkerke and David P. Kirkby. The RooFit toolkit for data modeling. *eConf*, C0303241:MOLT007, 2003.

[44] M. Kachelriess, Ricard Tomas, R. Buras, H.-Th. Janka, A. Marek, et al. Exploiting the neutronization burst of a galactic supernova. *Phys.Rev.*, D71:063003, 2005.

[45] Pasquale D. Serpico, Sovan Chakraborty, Tobias Fischer, Lorenz Hudepohl, Hans-Thomas Janka, et al. Probing the neutrino mass hierarchy with the rise time of a supernova burst. *Phys.Rev.*, D85:085031, 2012.

[46] Alessandro Mirizzi, G.G. Raffelt, and P.D. Serpico. Earth matter effects in supernova neutrinos: Optimal detector locations. *JCAP*, 0605:012, 2006.

[47] http://www.mpa-garching.mpg.de/ccsnarchive.

[48] Mathias Th. Keil, Georg G. Raffelt, and Hans-Thomas Janka. Monte Carlo study of supernova neutrino spectra formation. *Astrophys.J.*, 590:971–991, 2003.

[49] James T. Pantaleone. Neutrino oscillations at high densities. *Phys.Lett.*, B287:128–132, 1992.

[50] Stuart Samuel. Neutrino oscillations in dense neutrino gases. *Phys.Rev.*, D48:1462–1477, 1993.

[51] Alessandro Mirizzi and Ricard Tomas. Multi-angle effects in self-induced oscillations for different supernova neutrino fluxes. *Phys.Rev.*, D84:033013, 2011.

[52] Sovan Chakraborty, Tobias Fischer, Alessandro Mirizzi, Ninetta Saviano, and Ricard Tomas. No collective neutrino flavor conversions during the supernova accretion phase. *Phys.Rev.Lett.*, 107:151101, 2011.

[53] Srdjan Sarikas, Georg G. Raffelt, Lorenz Hudepohl, and Hans-Thomas Janka. Suppression of Self-Induced Flavor Conversion in the Supernova Accretion Phase.

[54] Amol S. Dighe and Alexei Yu. Smirnov. Identifying the neutrino mass spectrum from the neutrino burst from a supernova. *Phys.Rev.*, D62:033007, 2000.

Danksagung

An dieser Stelle möchte ich mich bei allen bedanken, die mich im Rahmen dieser Arbeit unterstützt haben.
Zunächst gilt mein Dank Caren Hagner für die Möglichkeit diese interessante Arbeit anzufertigen und für die Grundlage des guten Arbeitsklimas in dieser Gruppe.
Ganz besonderer Dank gilt Michael Wurm für die Betreuung dieser Arbeit, sein großes Engagement für LENA und sein liebenswürdiges Naturell.
Sebastian Lorenz danke ich für seine immer hilfsbereite Art bei Fragen aller Art, die Hilfestellungen und die konstruktive Kritik im Laufe dieser Arbeit.
Dank gilt Randolph Möllenberg für die Hilfe im Umgang mit der LENA Simulation und die ausführliche Beantwortung zahlreicher Fragen.
Ebenfalls bedanken möchte ich mich bei Lukas Hoppennau, auf dessen Arbeit teile dieser Arbeit aufbauen und der mir den Einstieg in das Thema erleichterte.
Das vielleicht größte Dankeschön gilt der gesamten Gruppe Neutrinophysik für die ständige Hilfsbereitschaft in allen Lagen, die regelmäßigen Köstlichkeiten in der Teeküche und das großartige Betriebsklima auf dem Flur: Joachim Ebert, Caren Hagner, Daniel Bick, Sebastian Lorenz, Michael Wurm, Christian Oldorf, Nadine Heidrich, Walter Schmidt-Parzefall, Björn Wonsak, Annika Hollnagel, Jan Timm, Volker Braunert, Laura Vanhoeffer, Henning Rebber, Benjamin Büttner, Mikko Meyer, Hans-Jürgen Ohmacht, Christoph Göllnitz und Jan Lenkeit. Ein zusätzlicher Dank gilt dem kickerenden Volk für die großartigen Spiele, ohne die der Büroalltag etwas grauer gewesen wäre. Volker danke ich darüberhinaus für das exzellente Büroklima.
Außerdem gilt mein Dank weiterhin den ehemaligen Gruppenmitgliedern: Martin Hierholzer, Torben Ferber, Marc Stöver, Manuel Harder und Philipp Neuhäußer.
Bedanken möchte ich mich außerdem bei Melleun, Malte, Fabian und Achim für die gemeinsame Zeit im Studium.
Schließlich danke ich meiner Familie, die mich stets auf meinen Wegen unterstützt hat.

Hiermit bestätige ich, dass die vorliegende Arbeit von mir selbständig verfasst wurde und ich keine anderen als die angegebenen Hilfsmittel – insbesondere keine im Quellenverzeichnis nicht benannten Internet-Quellen – benutzt habe und die Arbeit von mir vorher nicht einem anderen Prüfungsverfahren eingereicht wurde. Die eingereichte schriftliche Fassung entspricht der auf dem elektronischen Speichermedium. Ich bin damit einverstanden, dass die Masterarbeit veröffentlicht wird.

Hamburg, 11. Dezember 2012